Astronomy & Astrophysics manuscript no. output
April 4, 2022

Analysis of high-resolution FEROS spectroscopy for a sample of variable B-type stars assembled from TESS photometry*

Sarah Gebruers[1,2], Andrew Tkachenko[1], Dominic M. Bowman[1], Timothy Van Reeth[1], Siemen Burssens[1], Luc IJspeert[1], Laurent Mahy[3], Ilya Straumit[1,4], Maosheng Xiang[2], Hans-Walter Rix[2], and Conny Aerts[1,2,5]

[1] Institute of Astronomy, KU Leuven, Celestijnenlaan 200D, B-3001 Leuven, Belgium
e-mail: `sarah.gebruers@kuleuven.be`
[2] Max Planck Institute for Astronomy, Königstuhl 17, 69117 Heidelberg, Germany
[3] Koninklijke Sterrenwacht van België, Ringlaan 3, B-1180 Brussel, België
[4] The Department of Astronomy and Center of Cosmology and AstroParticle Physics, The Ohio State University, Columbus, OH 43210, USA
[5] Department of Astrophysics, IMAPP, Radboud University Nijmegen, PO Box 9010, 6500 GL Nijmegen, The Netherlands

Received XXX / Accepted XXX

ABSTRACT

Context. Spectroscopic data are necessary to break degeneracies in asteroseismic modelling of interiors of high- and intermediate-mass stars. With the TESS mission, the number of bright intermediate-mass B-type stars with long photometric light curves, that are therefore suitable for detailed asteroseismic studies, has increased significantly compared to the pre-TESS era.
Aims. We perform a homogeneous spectroscopic analysis for a sample of 166 B-type stars with TESS light curves to derive their surface characteristics. The variability types of these stars are also classified based on all currently available TESS sectors and ultimately prioritised according to their astrophysical potential.
Methods. We obtained high-resolution spectra for all 166 targets in the context of a large program with the FEROS spectrograph. The spectra are reduced with the CERES pipeline, for which we discuss several adaptations that we made to improve the quality of the reduced spectra. These optimally reduced stellar spectra are subsequently analysed with a machine learning-based spectrum analysis algorithm to infer precise stellar labels for all stars in the sample. Furthermore, the Least-Squares Deconvolution (LSD) method is employed to investigate spectral line profile variability (LPV) and isolate binary systems from apparently single stars.
Results. The LSD profile analysis leads to identification of 26 spectroscopic double-lined binaries, 42 supergiants in the Large Magellanic Cloud galaxy, and 98 Galactic stars, both with and without apparent LPV. For the Galactic single stars and single-lined spectroscopic binaries, we determine their five main surface parameters: effective temperature ($T_{\rm eff}$), surface gravity ($\log g$), global metallicity ([M/H]), projected rotational velocity ($v \sin i$), and microturbulent velocity (ξ) with average precisions of 70 K, 0.03 dex, 0.07 dex, 8 km s^{-1}, and 0.7 km s^{-1} respectively. The average internal uncertainties we find for FEROS spectra with our spectrum analysis method are 430 K ($T_{\rm eff}$), 0.12 dex ($\log g$), 0.13 dex ([M/H]), 12 km s^{-1} ($v \sin i$), and 2 km s^{-1} (ξ).
Conclusions. We discover 13 new HgMn stars in the Galactic sample, of which only one is found in a spectroscopic binary. Moreover, we find spectroscopic evidence that eight of the 98 galactic single or SB1 variables are fast rotating gravity-mode pulsators occurring in between the SPB and δ Sct instability strips. The g-mode frequencies of these pulsators are shifted to relatively high frequency values due to their rotation, and their apparently too low effective temperatures relative to the SPB instability region can in most cases be explained by the gravity darkening effect.

Key words. asteroseismology – stars: variables: general – stars: oscillations – stars: fundamental parameters – techniques: spectroscopic

1. Introduction

While massive stars are important suppliers of chemical and mechanical feedback to the interstellar medium (e.g. Langer 2012), their structure and evolution is not yet well understood. Large theoretical uncertainties occur already during the early phases, that have an impact on the further evolution (e.g. Maeder & Meynet 2000; Ekström et al. 2012; Aerts et al. 2019). To calibrate physical processes in these stars, observational constraints from their interiors are needed. With space asteroseismology, observed pulsations inside stars provide information about stellar interiors (Aerts 2021). Low-mass stars pulsate with pressure modes (p-modes) that probe the stellar envelope. They have a similar structure to that of the Sun, thus similar analysis techniques can be used as in helioseismology (Christensen-Dalsgaard 2002). On the other hand, intermediate to massive main-sequence stars (M ~ 3-25 $M_\odot$) pulsate both in p- and g-modes, either simultaneously (the case of hybrid pulsators) or separately. Gravity-mode oscillations are most sensitive to physical conditions in the near-core regions of stars with M > 1.3 $M_\odot$, and are therefore ideal to unravel the mechanisms of convective core boundary mixing, near-core rotation and chemical mixing (see Bowman 2020 for a review). Many theoretical and observational studies of single stars or their ensembles have used g-mode pulsations to infer internal information such as the profile of the convective boundary mixing region and the radiative envelope, the internal rotation rate, and the amount of chemical mixing, both in slowly pulsating B stars (SPB) and β Cephei (β Cep) stars

---

* Based on observations collected at the European Southern Observatory, La Silla, Chile under program 0104.A-9001(A).

(e.g. Miglio et al. 2008; Szewczuk & Daszyńska-Daszkiewicz 2015; Moravveji et al. 2016; Pedersen et al. 2018; Michielsen et al. 2019; Moździerski et al. 2019), and in less massive γ Doradus (γ Dor) stars (e.g. Van Reeth et al. 2018; Mombarg et al. 2020; Angelou et al. 2020).

There are not that many asteroseismic studies of massive stars, as compared to low-mass stars, because long time base, continuous and high-precision time series are needed to properly resolve frequencies and identify geometries of g-mode pulsations (Bowman 2020). This became possible with the start of science operations of space missions such as CoRoT (Auvergne et al. 2009) and *Kepler* (Borucki et al. 2010). Especially the *Kepler* mission revolutionised the field of g-mode asteroseismology with its four-year duration light curves. However, *Kepler* was pointed to one fixed field of view for its entire nominal mission duration, where the field selection was driven by the primary science of the mission of detection and characterisation of exoplanets around solar-like stars. Therefore, not many massive stars were observed by the mission. The ongoing Transiting Exoplanet Survey Satellite (TESS) mission (Ricker et al. 2015) is observing the whole sky searching for planets around bright stars, and thereby also targeting O- and B-type stars. The nominal mission divided the two ecliptic hemispheres into 13 sectors that are each observed for 27 days. The 13 sectors in the Northern and Southern ecliptic hemispheres overlap near the poles where one-year long observations are taken. In the Southern hemisphere, the TESS continuous viewing zone (CVZ) includes the Large Magellanic Cloud (LMC) galaxy which means that different metallicity regimes can be probed. Different studies have demonstrated the diverse variability among OB-type stars using Kepler/K2 and TESS light curves. Bowman et al. (2019b) and Burssens et al. (2019) found a number of coherent pulsators among more than 100 OB-type stars in the K2 mission, and light curves dominated by stochastic low-frequency variability (SLF) for the most massive stars and dozens of blue supergiants observed with K2 and TESS. From the first two sectors of TESS, Pedersen et al. (2019) detected and classified the variability for a sample of 154 OB-type stars, including 40 LMC targets, showing that 90% have pulsational, binary, rotational or SLF variability. Burssens et al. (2020) also found a large diversity of variability in a sample of OB-type stars observed within the first 13 sectors of TESS, and demonstrated the power of coupling TESS light curves with high-resolution spectroscopy.

Asteroseismic modelling of intermediate-mass stars entails a number of degeneracies due to strong correlations between the numerous parameters occurring in stellar models. The addition of spectroscopic, binarity or astrometric data helps to lift these degeneracies, reduce uncertainties on the parameters, and supplies information that is required to establish a link between interiors of stars and their atmospheric layers. With this in mind, many studies in the past decade have focused on obtaining spectroscopic parameters for samples of promising pulsating *Kepler* stars (e.g., Lehmann et al. 2011; Tkachenko et al. 2012, 2013b,a; Van Reeth et al. 2015; Niemczura et al. 2015, 2017). In recent years, detailed asteroseismic modelling of intermediate-mass stars has made advances by including non-photometric data. For example, Mombarg et al. (2019) added spectroscopic measurements of the effective temperature ($T_{\rm eff}$) and surface gravity ($\log g$) to the forward modelling of γ Dor stars to lift degeneracies and to estimate masses and ages of stars. In Mombarg et al. (2020), atomic diffusion in AF-type stars was studied by not only adding spectroscopic $T_{\rm eff}$ and $\log g$ values to g-mode asteroseismic modelling, but also by comparing the predicted surface abundances with observational ones to evaluate models with and without atomic diffusion. Pedersen et al. (2018) studied different mixing profiles in more massive B-type stars and emphasised importance of adding surface abundances to asteroseismic modelling to constrain the shape of the mixing profiles in radiative zones of these stars. Pedersen et al. (2021) performed forward asteroseismic modelling on a sample of 26 SPB stars where they applied spectroscopic parameters and an astrometric measurement of the luminosity to delimit the parameter space. Aside from spectroscopy, binary modelling can also add valuable constraints to asteroseismic modelling since it can deliver independent estimates of the radius and mass with very high precision. Johnston et al. (2019), for example, used binary information to reduce parameter uncertainties and correlations between parameters in the modelling of binaries with g-mode pulsators. Sekaran et al. (2020, 2021) combined *Kepler* photometry with high-resolution optical HERMES spectroscopy (Raskin et al. 2011) to perform a detailed asteroseismic study of a γ Dor-type g-mode pulsator in an eclipsing SB2 binary system. The authors demonstrated that it is highly beneficial for asteroseismic modelling to add model-independent information on stellar mass and radius inferred from binary dynamics.

In addition to asteroseismology, the analysis of stellar atmospheres with spectroscopy is also an important tool to obtain information about stars and to calibrate theoretical models. By combining these two techniques, greatly improved theoretical constraints can be obtained since both the surface and the interior are probed. During early phases of the *Kepler* mission science operations, ground-based spectroscopy was frequently used in tandem with *Kepler* photometry to aid with the photometric classification of variable stars. $T_{\rm eff}$ and $\log g$ estimates were used to place stars in the Kiel diagram and compare their positions with theoretical instability strips of different types of pulsators, thus confirming or rejecting the photometric classification (e.g. Uytterhoeven et al. 2011; Balona et al. 2011; Tkachenko et al. 2013a). The spectroscopic surface measurements were also used to check estimates of those parameters determined from photometry (e.g. Silva Aguirre et al. 2012; Thygesen et al. 2012; Pinsonneault et al. 2014). The other way around, asteroseismic values of the surface gravity are often more precise than spectroscopic ones and have thus been used in some studies to better constrain spectroscopic surface parameters of stars (Bruntt et al. 2012; Thygesen et al. 2012).

In this paper, we analyse the spectra of 166 B-type stars that exhibit photometric variability in their TESS light curves, with the purpose of future combined asteroseismic and spectroscopic modelling. For the sake of efficiency and consistency of the obtained results across the entire stellar sample, we employ the ZETA-PAYNE (Straumit et al. 2022) machine learning-based spectrum analysis algorithm. The method is a generalisation of the originally proposed THE PAYNE algorithm (Ting et al. 2019) towards inclusion of a model of a priori unknown residual response function of the instrument into the parameter vector. This way, parameters of the residual response function are optimised along with the atmospheric parameters of the star, thus removing the need to normalise stellar spectra manually in advance. In Sect. 2, we discuss the sample selection and observations of the targets. We describe some improvements made to the spectrum reduction pipeline in Sect. 3. The spectroscopic classification is presented in Sect. 4 along with a summary of the ZETA-PAYNE framework and a few tests for the specific setup of this paper. The spectroscopic and photometric results are given in Sect. 5, while the internal uncertainties of the methodology and the specific case of peculiar stars are discussed in Sect. 6. The same section presents the obtained results in the context of the spectroscopic Hertzsprung-Russell diagram (Langer & Kudritzki 2014). We conclude our study in Sect. 7.

2. Sample selection and observations

We selected all the bright targets (stars with magnitudes in the V-band below 11.5) in the samples of variable OB-type stars from Pedersen et al. (2019) and Bowman et al. (2019b). These samples were constructed following the asteroseismic potential of OB-type stars as determined from the first three TESS sectors that were available at that time. For the 166 brightest stars, we obtained spectroscopic observations with the Fibre-fed Extended Range Optical Spectrograph (FEROS, Kaufer et al. 1999) which is attached to the ESO/MPG 2.2-m telescope at La Silla, Chile. In an accompanying paper (Serebriakova et al. in prep.), the spectroscopic analysis of ESO UVES spectra for fainter stars (Vmag > 11.5) from the samples of Pedersen et al. (2019) and Bowman et al. (2019b) will be presented.

FEROS is a high-resolution spectrograph (R ∼ 48 000) that covers a wavelength range from 3600-9200 Å over 39 orders. The observations were taken during December 2019 and February 2020. In total 166 objects were observed with a minimum of two epochs per target (separated by two months), except for seven targets that were not observable during the second run in February. The spectra were reduced with the publicly available Collection of Elemental Routines for Echelle Spectra (CERES, Brahm et al. 2017)[1]. This package consists of automated reduction pipelines for 13 different échelle spectrographs, among which FEROS. The pipelines are written in `Python` and complemented with `C` and `Fortran` routines to speed-optimise the time consuming parts. It performs a bias subtraction, correction for bad columns, background subtraction, order extraction, wavelength calibration, barycentric correction and a blaze correction. To achieve the goals of this paper, some changes to the CERES pipeline were necessary to obtain most optimally extracted 1D spectra. These changes are described in Sect. 3.

To complement the spectroscopic data within this work and to classify the dominant variability type of each target, we reanalysed available 2-min cadence photometry from TESS. We downloaded the available simple aperture photometry (SAP) and pre-data search conditioning (PDC-SAP) light curves output from the NASA SPOC pipeline (Jenkins et al. 2016) from the Mikulsi Archive for Space Telescopes (MAST[2]). Almost all bright ($V \leq 14$ mag) O and early-B stars observed by TESS were prioritised for 2-min cadence in at least one sector because of successful guest investigator proposals[3]. Yet, some stars fall between the gaps in the CCDs and cameras, or are located close to the ecliptic. Cycle 4 of the TESS mission is currently in progress as of July 2021, which includes the second visit to the northern ecliptic hemisphere and parts of the ecliptic for the first time.

(Almost) all of our targets currently have at least one sector of TESS data available, which is sufficient to classify its dominant variability. Given that variability classification is sufficient for this paper, as its focus is on the analysis of the newly-obtained spectroscopic data for a large number of B-type stars, we focused our photometric analysis on the longer time spans of 2-min TESS light curves available for each target. We checked both the available SAP and PDC-SAP light curves to compare and contrast the impact of instrumental systematics that may be present in either or both light curve formats. In most cases, the latter were sufficient for variability classification. However, we note that correcting for instrumental effects (e.g. extracting custom light curves) to derive reliable lists of pulsation frequencies is the subject of future work.

3. Improvements of the CERES pipeline for the FEROS spectra

The CERES pipeline reduces 25 of the 39 FEROS orders, which corresponds to the wavelength range 3800-6800 Å, containing six Balmer lines and sufficient metal lines to determine stellar parameters (Brahm et al. 2017). We made four changes to the existing CERES pipeline in order to meet our quest for high-precision spectroscopic parameter determination of our targets. The first two were necessary to remove unphysical artefacts (hereafter referred to as wiggles) from the spectra and to eliminate 'bumps' occurring at the edges of the orders. The other two changes concern an additional function that merges the individual orders and a method to remove cosmic hits. The original CERES pipeline only returns separate orders and not the fully merged spectrum since the main purpose of the developers was to determine precise radial velocities which is possible from individual orders.

When obtaining reduced spectra with the original CERES pipeline, we detected wiggles and a gap at certain positions in the 1D spectra (see the arrows in the top panel of Fig. 1). We traced these features back to bad columns in the 2D frames. The original pipeline corrects for the bad columns by interpolating among the good pixels in each row at the positions of the bad pixels. However, because the orders are skewed, some parts of the bad columns are assigned too much or too little flux in this way, creating the observed wiggles in the 1D spectra. Instead of interpolating within each row, we found that almost all the bad columns disappear when the bias frame is subtracted from the observed science frames. The bias frame contains the same bad columns as the science frames so when the first one is subtracted from the latter, the excess in flux is removed and the bad columns are no longer visible in the 2D frames. This is the case for all but one bad column. Column 1299 is the brightest one present in the 2D frames and does not disappear by subtracting the bias. For the pixels in this column we increased the variance by 10 000 such that they have an extremely small weight and almost no contribution in the extraction process.

The original CERES pipeline corrects for the blaze function by dividing each individual order by the normalised flat field in that order. The normalised flat field is assumed to represent the blaze function according to Brahm et al. (2017), and is defined as the flat field divided by its maximum in that order. However, we noticed that this blaze correction induces large intensity jumps or 'bumps' where successive orders overlap (see yellow circles in the top panel of Fig. 1). When instead the orders are divided by the non-normalised flat field, they connect much better and bumps are no longer visible (see bottom panel of Fig. 1). Therefore we changed the blaze correction in CERES to a division of each spectral order by the non-normalised flat field.

The CERES pipeline only outputs the 1D spectrum for individual orders. While this is fine for radial velocity determinations, for which the pipeline was designed, we needed the whole spectrum to perform a spectral analysis. Therefore, we implemented order merging into the code. First we created a unified wavelength grid in logarithmic scale that covers the full wavelength range of all the extracted orders and has a relative step-

---

[1] https://github.com/rabrahm/ceres

[2] https://archive.stsci.edu/

[3] GO3059 and GO4074; PI: Bowman; https://heasarc.gsfc.nasa.gov/docs/tess/approved-programs.html

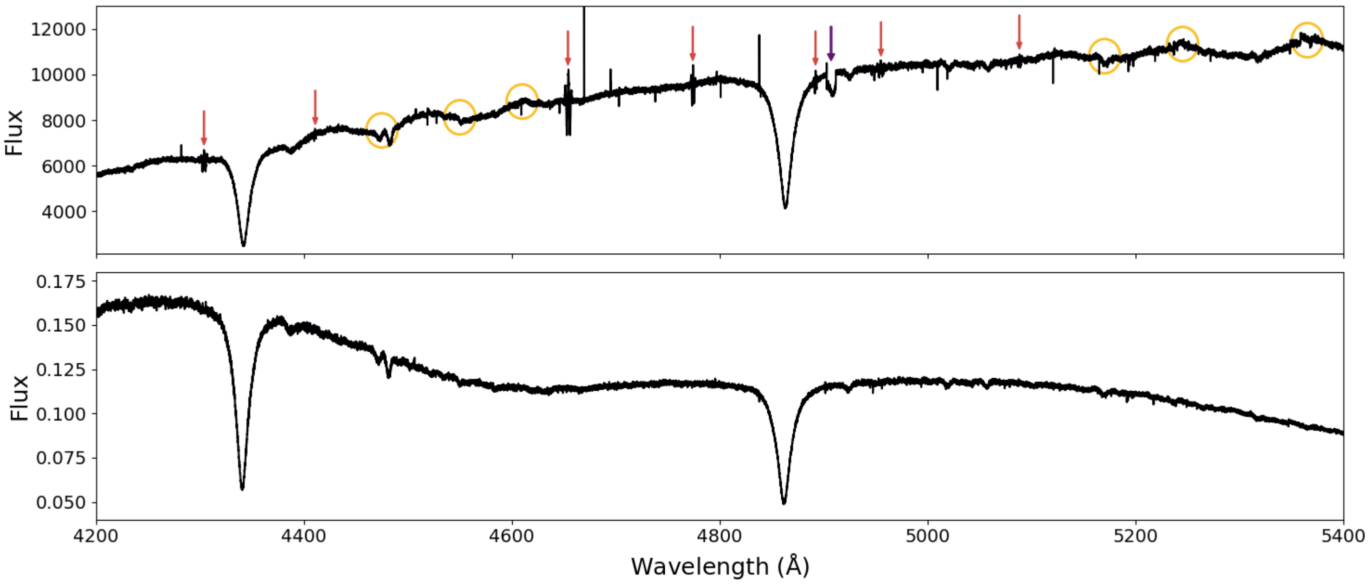

Fig. 1: *Top:* spectrum of B9V star HD 33244 reduced with the original CERES pipeline. Red and purple arrows indicate the positions of wiggles and a gap, yellow circles show the positions of some bumps (see text for explanation). *Bottom:* spectrum of HD 33244 reduced with the new version of the CERES pipeline that includes the four changes described in Sect. 3.

size of 10^{-5}. This stepsize is approximately equal to $1/(2R)$ with R the resolution of FEROS ($R = 48\,000$). Each order was then shifted to the new wavelength grid by linear interpolation. We merged the orders by taking a weighted sum, with as weight the square of the signal-to-noise ratio ($w = (\mathrm{S/N})^2$):

$$f_{merged} = \frac{\sum_i f_i w_i}{\sum_i w_i} \quad \text{and} \quad \sigma_{f_{merged}} = \frac{\sqrt{\sum_i \sigma_{f,i}^2\, w_i^2}}{\sum_i w_i}, \tag{1}$$

where f_i is the blaze corrected flux in order i and $\sigma_{f,i}$ is its uncertainty. If pure Poisson noise is assumed, $(\mathrm{S/N})_i^2$ is equal to the number of photons from the star in a certain order so that the weighted mean in Eq. 1 is just a co-addition of photons over all orders. This means that in overlapping neighbouring orders, where part of the photons had ended up in one or the other order, all photons are added again by Eq. 1.

We added two steps to the pipeline to remove sharp lines originating from cosmic rays and chip defects. In the first step we only dealt with positive hits due to cosmic hits. At every position in the spectrum we computed the median flux and standard deviation within a window of 100 pixels (~ 5Å). When the difference between the flux at that point and the median flux was larger than four times the standard deviation, the flux value was replaced with the median value. This process was repeated five times. The second step also removed negative hits due to chip defects, but here the method was more conservative to prevent removing stellar absorption lines. This is especially difficult in slowly rotating stars that have many narrow absorption lines that must not be mistaken for cosmic hits. The method is the same as for the positive cosmic hits, only the window size was changed to 30 pixels (~ 1.5Å) and both positive and negative hits were removed.

4. Analysis methods

4.1. Spectroscopic classification

To make a spectroscopic classification of the sample, the reduced spectra were subjected to least-squares deconvolution (LSD; Donati et al. 1997). We produced LSD profiles using the method of Tkachenko et al. (2013c)[4]. The computation of LSD profiles requires normalised spectra and spectral line masks. Therefore, we ran each individual spectrum through the ZETA-PAYNE setup, which is described in Sect. 4.2, and obtained normalised spectra from which the response function is removed. The line masks were computed with the GSSP code (Tkachenko 2015), which relies on atmosphere models obtained with the LLmodels code (Shulyak et al. 2004), the radiative transfer code SynthV (Tsymbal 1996), and Vienna Atomic Line Database (VALD, Kupka et al. 1999) atomic data. For each star we computed a GSSP model for its preliminary $T_{\rm eff}$ and $\log g$ returned by the ZETA-PAYNE, and we fixed [M/H] to 0 dex.

We identified double-lined spectroscopic binaries (SB2s) as stars for which two components could be distinguished in the LSD profiles, while in some cases also revealing different relative positions of the spectral lines of the two components for the different epochs of that target. The LSD profiles were also used to detect line profile variability (LPV), which may be caused by various physical origins, such as chemical inhomogeneities or pulsations. Examples of LSD profiles for an SB2 system and a star with LPV are shown in Fig. 2. In total 26 targets were classified as SB2 systems or as targets for which it was not clear whether the variability in the LSD profiles is due to binarity or LPV. Some of these systems were already identified as (spectroscopic) binaries in SIMBAD. These 26 targets were excluded from the sample since they require the (simultaneous) analysis of both components, which is not yet possible with our current method. They are listed as SB2 systems in Table 5.

---

[4] `https://github.com/TVanReeth/Least-squares-deconvolution`

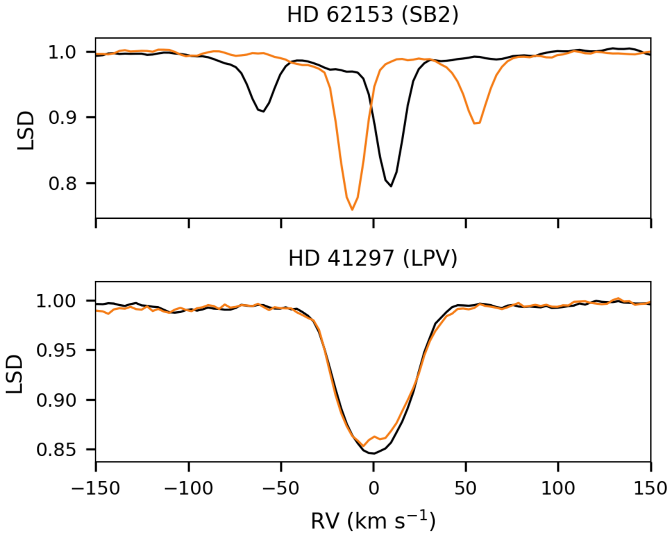

Fig. 2: *Top:* LSD profiles for two epochs of SB2 system HD 62153. *Bottom:* LSD profiles for two epochs of single star HD 41297 with LPV.

The remaining targets were divided into two groups based upon the LPV in the different epochs of each target. The first group consists of 42 stars with LPV, either in H$_\alpha$, in all Balmer lines or also metal lines. Two of these stars are Be stars with not only Balmer lines in emission but also metal emission lines. The other 40 stars are classified as (blue) supergiants in SIMBAD and all of them are members of the LMC. For this type of star, non-local thermodynamic equilibrium (NLTE) analysis including wind physics is required to obtain atmospheric parameters. Our current setup of the ZETA-PAYNE is trained on LTE model spectra for log $g > 3$ dex, while supergiants typically have log g values between 1 and 3 dex. Therefore it could not be applied to the spectra of the supergiants. Instead, these 42 stars will be studied in the complementary paper by Serebriakova et al. (in prep.) focused on OBA-type supergiant LMC members.

The other group contains 92 stars without clear LPV or having variability in the metal lines but stable Balmer lines, as well as six Be stars with Balmer lines in emission. These 98 (Galactic) stars are further studied in this paper. Among them, we identified single-lined spectroscopic binaries (SB1s) using the radial velocity (RV) determinations from the ZETA-PAYNE. A target was classified as SB1 system when the RV difference between any two epochs of that target is larger than the uncertainties of the RV values. We do remark that this RV difference might also be caused by pulsations. If the RV differences are smaller than the uncertainties or when there is only one spectrum available, the star was assumed to be single. Twelve targets were found to be SB1 systems and 86 are single stars.

For each of the targets, we shifted all of its spectra to RV = 0 km s^{-1} and added them by taking a weighted sum, where the weight of each epoch is the square of the S/N value of that epoch computed following the algorithm from Stoehr et al. (2008). We subsequently used that same algorithm to compute the S/N of the averaged spectrum; these values are reported in column 3 of Table 6. The number of epochs and binary information are given in columns 2 and 4 of the same table.

Table 1: Parameter ranges of the training grid.

Parameter	Quasi-random grid	Oversampled grid
T_{eff} (K)	6000 - 25 000	N(6000, 4000)
log g (dex)	3 - 5	3 - 5
[M/H] (dex)	-0.8 - 0.8	-0.8 - 0.8
$v \sin i$ (km s^{-1})	0 - 400	N(0, 25)
ξ (km s^{-1})	0 - 20	0 - 20

4.2. Spectrum analysis with the ZETA-PAYNE

We use the ZETA-PAYNE (Straumit et al. 2022) spectrum analysis algorithm to analyse the averaged spectra of the 98 Galactic single stars or SB1 systems. The ZETA-PAYNE is a machine learning framework that trains a neural network on a grid of synthetic spectra to obtain a spectrum interpolator. This interpolator predicts theoretical flux spectra for an arbitrary set of stellar labels and can be used to fit any observed spectrum and derive its surface parameters as long as they are within the parameter ranges of the training sample.

In this paper, the neural network was trained with 1D LTE synthetic models computed with GSSP. Instead of using a regular grid in five dimensions — one for each of the parameters we want to determine, namely T_{eff}, log g, global metallicity ([M/H]), projected rotational velocity ($v \sin i$) and microturbulent velocity (ξ) — we created a grid that is quasi-randomly spaced using Sobol numbers (Sobol 1967). It covers the whole parameter space for main sequence BAF-type stars as listed in the second column of Table 1, but with fewer grid points than a regular grid would need and is therefore more feasible to compute. Straumit et al. (2022) point out that, for high-resolution spectra, the neural network performs worse in regions of the parameter space with low values of $v \sin i$ and temperatures in the late-A to F-type regime. This is due to the many narrow spectral lines that have to be resolved by the neural network in this regime. To improve the performance of the neural network for such complex spectra, the parameter space should be oversampled with model spectra computed for low $v \sin i$ and low T_{eff} values. The final training sample therefore consists of 5000 quasi-randomly spaced model spectra and 5000 additional random model spectra with T_{eff} and $v \sin i$ drawn from the normal distributions N(6000, 4000) and N(0, 25) respectively. An overview of the parameter ranges for the whole training grid is given in Table 1.

All the model spectra were computed within the wavelength range from 3000 to 10 500 Å and for infinite resolution (no instrumental broadening) such that the grid can also be used for optical spectra from spectrographs other than FEROS. During the fitting procedure the spectra are convolved to the resolution of the respective spectrograph by either using a constant resolution value or a wavelength dependent resolution (the line spread function, LSF). We used the constant resolution value of FEROS ($R = 48\,000$), because the LSF computed from the ThAr frames that were taken during the observing run, changes from night to night. The training of the neural network was done identical to the procedure described in Straumit et al. (2022), so more information can be found in that paper. For every star in the sample, surface parameters and the radial velocity were derived by fitting model spectra to the observed spectrum using the neural network interpolator, performing a Doppler shift, and minimising the χ^2 merit function. However, the neural network was trained on continuum normalised spectra while the observed spectra contain components from the instrument (the response function), the interstellar medium (ISM) and the Earth's atmosphere. Each observed spectrum had to be divided by its response function before it could be compared to the normalised model spectra. In the ideal case, the response function of a spectrograph is known and can be removed from any observed spectrum to obtain only the component from the star itself (and some additional features from the ISM and the Earth's atmosphere such as telluric lines). This is attempted by dividing an observed spectrum by a flat-field exposure, but some curvature always remains in the spectrum that is not related to the stellar atmosphere (Gray 2005, Chap. 12). In practice, the response function is mostly removed by fitting a spline or a polynomial to manually selected points that are assumed to be part of the continuum. This is a rather subjective way of normalising a spectrum and can give different results when it is done by different researchers.

In order to minimise subjectivity, we followed Straumit et al. (2022) and normalised the spectra automatically during the fitting procedure in the ZETA-PAYNE, such that the optimal response function was determined simultaneously with the best-fitting surface parameters. We assumed that the response function could be represented by a Chebyshev polynomial for which we optimised its coefficients (as described in Straumit et al. 2022). The number of coefficients is a free parameter that had to be fixed before starting the fitting procedure. Preferably the number is as small as possible to ensure that no features are introduced into the spectrum, but it should also be high enough to capture the whole shape of the response function. It also depends on the wavelength range, where generally more coefficients are needed when a longer wavelength range is used. For our analysis, we selected a wavelength range from 4000 to 5800 Å because (i) it includes three Balmer lines (H_β, H_γ and H_δ), (ii) many metal lines, but (iii) excludes H_α region that complicates the optimal normalisation of FEROS spectra. Since all the response functions of the FEROS spectra have a similar shape, the same number of Chebyshev coefficients could be used for all the stars.

We tested the optimal number of Chebyshev coefficients for a typical FEROS response function by taking five random stars from the sample for which we fitted the spectra with 10, 15, 20, 25, 30 and 35 coefficients with the ZETA-PAYNE. For each fit we computed the χ^2 value and plotted those values as a function of the number of coefficients (see Fig. 3). The χ^2 profile converges towards a certain value and this plateau is reached around 25 coefficients. Therefore, we used 25 Chebyshev coefficients to represent the FEROS response functions.

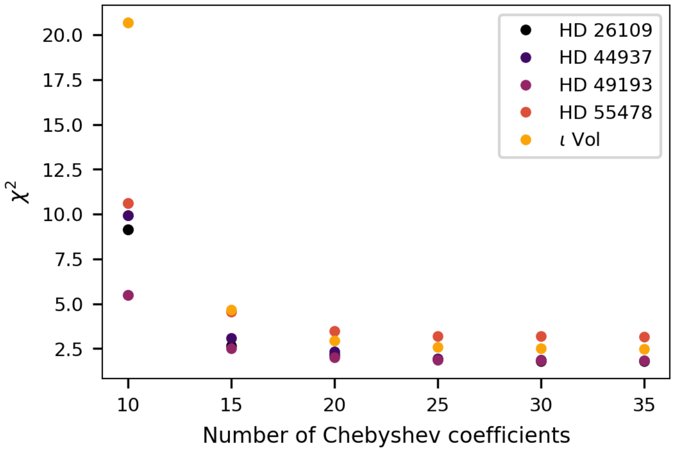

Fig. 3: χ^2 values for best-fitting synthetic spectra to the observed spectra of five sample stars as a function of the number of Chebyshev coefficients.

Table 2: Average internal uncertainties for the surface parameters and the radial velocity computed from 1000 simulated FEROS spectra, without noise and for S/N = 150.

	Internal uncertainty	
Parameter	noiseless	S/N = 150
$T_{\rm eff}$ (K)	430	425
log g (dex)	0.12	0.12
v sin i (km s^{-1})	12	12
ξ (km s^{-1})	2.20	2.25
[M/H] (dex)	0.13	0.13
RV (km s^{-1})	0.96	0.97
Reliability	94.6%	94.3%

4.3. Internal uncertainties

We determined the internal uncertainties of the stellar parameters that are inherent to the modelling setup. We created 1000 artificial FEROS spectra in the wavelength range from 4000 to 5800 Å, quasi-randomly spaced within the parameter space but not overlapping with the training sample. Each spectrum was computed with GSSP, given a random radial velocity shift within ± 50 km s^{-1}, and convolved to the resolution of FEROS. A random response function was introduced represented by a Chebyshev polynomial with 25 coefficients. For every spectrum we got a noiseless version and a version with S/N = 150, a typical value for the real FEROS spectra. All the artificial spectra were analysed with the fitting routine of the ZETA-PAYNE and the resulting parameters were compared with their real values. Outliers were identified as spectra for which the temperature difference was larger than four times the 1σ standard deviation of the temperature difference distribution of all 1000 spectra. This is formulated as the reliability fraction of the neural network (Straumit et al. 2022) and is given in the last row of Table 2.

Using only the remaining spectra without the outliers, we computed the internal uncertainty for each parameter as the mean difference between the real values and the ones obtained with the ZETA-PAYNE. These uncertainties for noiseless spectra and for spectra with S/N = 150 are given in Table 2, and should be taken into account when determining parameters for the observed FEROS spectra.

4.4. Effect of the selected wavelength region

The atmospheric parameters of the main sequence stars in our sample were derived using the spectral wavelength range 4000-5800 Å. To test whether the analysis of a longer or shorter wavelength range has any effect on the obtained parameters, we selected six stars distributed over the parameter space and applied the ZETA-PAYNE on three different wavelength ranges. The wavelength ranges are: 3870-6750 Å (H_α, H_β, H_γ, H_δ, and H_ϵ), 3870-5800 Å (H_β, H_γ, H_δ, and H_ϵ), and 4200-5800 Å (H_β and H_γ). For each of these wavelength ranges, we computed the difference in parameters with those obtained from the original wavelength range (4000-5800 Å). This is shown in Fig. 4. All the values lie within the internal uncertainties from Table 2. This demonstrates that the choice of wavelength region has no statistically significant effect on the surface parameters when the internal uncertainties are taken into account.

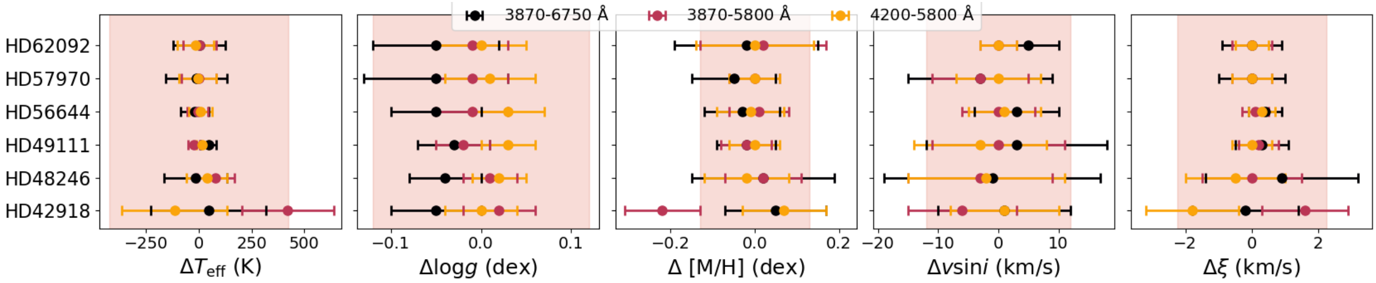

Fig. 4: Comparison of stellar parameters derived from different wavelength regions. From left to right the differences in $T_{\rm eff}$, $\log g$, [M/H], $v \sin i$ and ξ are shown. Black, red and yellow dots are the differences between the parameter value obtained from the 4000-5800 Å spectral range and the parameter value obtained from the wavelength range indicated with the respective colour in the legend of the figure, so $p_{4000-5800\text{Å}}$ - $p_{\Delta\lambda}$. The pink region indicates the internal uncertainty interval from Table 2.

We noticed that the uncertainties on the surface parameters increase with longer wavelength regions. There is also a trend of increasing $\log g$ when a longer wavelength region is analysed, although all values are still within the internal uncertainties. This is caused by the normalisation of the spectrum, which becomes more difficult when more parts of the spectrum are included. Especially when H_α is included, a wavelength range containing multiple telluric lines is covered. The ZETA-PAYNE cannot model these. For the stars in Fig. 4, we found that for longer wavelength regions, the wings of the Balmer lines get more broadened than when shorter wavelength regions are analysed with the ZETA-PAYNE. This is demonstrated in Fig. 5 and shows that our normalisation approach with a Chebyshev polynomial of 25 coefficients is not optimised to normalise a spectrum extended to H_α or to H_ϵ, and that the deterioration in normalisation of the Balmer wings gets compensated by preferring a model with higher $\log g$. Additional tests for the number of Chebyshev coefficients and methods to remove tellurics are needed to get a better normalisation in each specific wavelength range. Here we decided to limit our analysis to the 4000-5800 Å region since not that much information is added by extending to H_ϵ and normalisation becomes much more uncertain when including H_α.

5. Analysis results

5.1. Spectroscopy

The results for the 98 stars analysed with ZETA-PAYNE are given in Table 6. The statistical uncertainties inferred from using ZETA-PAYNE (Δ) and those that include the internal uncertainty ($\Delta_{\rm i}$) are also provided. We advise to use the latter value since they are more representative for the typical precision with which the surface parameters of B-type stars can be derived. The distributions of the surface parameters are shown in grey in Fig. 6. Most of the stars have parameters indicative of late B-type, with temperatures in the range 10 000-14 000 K. There are some cooler stars (early A-type) in the sample and a few hotter stars with $T_{\rm eff}$ > 16 000 K. From the $\log g$ distribution it can be seen that the majority are main-sequence stars. However, there are six stars with $\log g < 3.5$ dex indicating that these are near the end or just beyond the main sequence. The $v \sin i$ values are fairly uniformly distributed within 0-350 km s^{-1} and the metallicity shows a normal distribution around solar value with mean of (-0.12 ± 0.27) dex.

All the fits with the ZETA-PAYNE were visually inspected. For 20 stars we noticed that the model predicted by the ZETA-PAYNE as best fitting model does not fully correspond to the observed spectrum. In 13 of those cases, the observed spectrum contains more absorption lines than the predicted spectrum. These stars were identified as chemically peculiar, and specifically HgMn stars, which are further discussed in Sect. 6.2. Three stars (HD 40435, HD 45527, and HD 63928) show strong LPV in their spectra and four other ones (CPD-60 944B, HD 32493, HD 59426, and HD 6783) have very narrow spectral lines with strongly variable depths between different epochs. These stars are indicated as ‘LPV’ and ‘LPV*’, respectively, in Table 6. From the TESS light curves discussed in the following section, we find that these seven stars are rotational variables. This means that they are likely chemically peculiar (that is, CP2 stars), which explains the limited agreement with the best fitting model spectra. In many of these stars Cr is overabundant, confirming the chemically peculiar nature. An in-depth chemical abundance analysis is beyond the scope of this work.

5.2. Variability classification from TESS Photometry

We analysed both SAP and PDC-SAP light curves independently for all stars to gauge the possible effect of systematics, and we checked that the allocated aperture mask and background pixels by the SPOC pipeline are reasonable. It has been shown that, for example, SAP light curves are preferable in the identification and analysis of bright eclipsing binaries (see e.g. Southworth et al. 2020, 2021). For each star, we calculated the amplitude spectrum of its SAP and PDC-SAP light curves using a discrete Fourier transform (DFT; Kurtz 1985) up to the Nyquist frequency, which for the 2-min TESS data is 360 d^{-1}. A high diversity and incidence of photometric variability occurs in massive stars, with common causes including pulsations, rotational modulation, winds and binarity (Pedersen et al. 2019; Bowman et al. 2019a,b, 2020; Burssens et al. 2020). Based on a group of expert classifiers, we visually inspected the light curves and amplitude spectra and determined the dominant variability type(s), which is included in Table 5.

Of particular interest are stars pulsating in coherent p and/or g modes for follow-up asteroseismic modelling (e.g. Moravveji et al. 2015, 2016; Szewczuk & Daszyńska-Daszkiewicz 2018; Szewczuk et al. 2022; Pedersen et al. 2021), (pulsating) eclipsing binaries (e.g. Tkachenko et al. 2020; Sekaran et al. 2020, 2021) and stars with stochastic low-frequency variability caused by gravity waves (e.g. Bowman et al. 2019b, 2020). A full list of all variability types used in this work, which are not mutually exclusive, include:

- rot: rotational modulation;

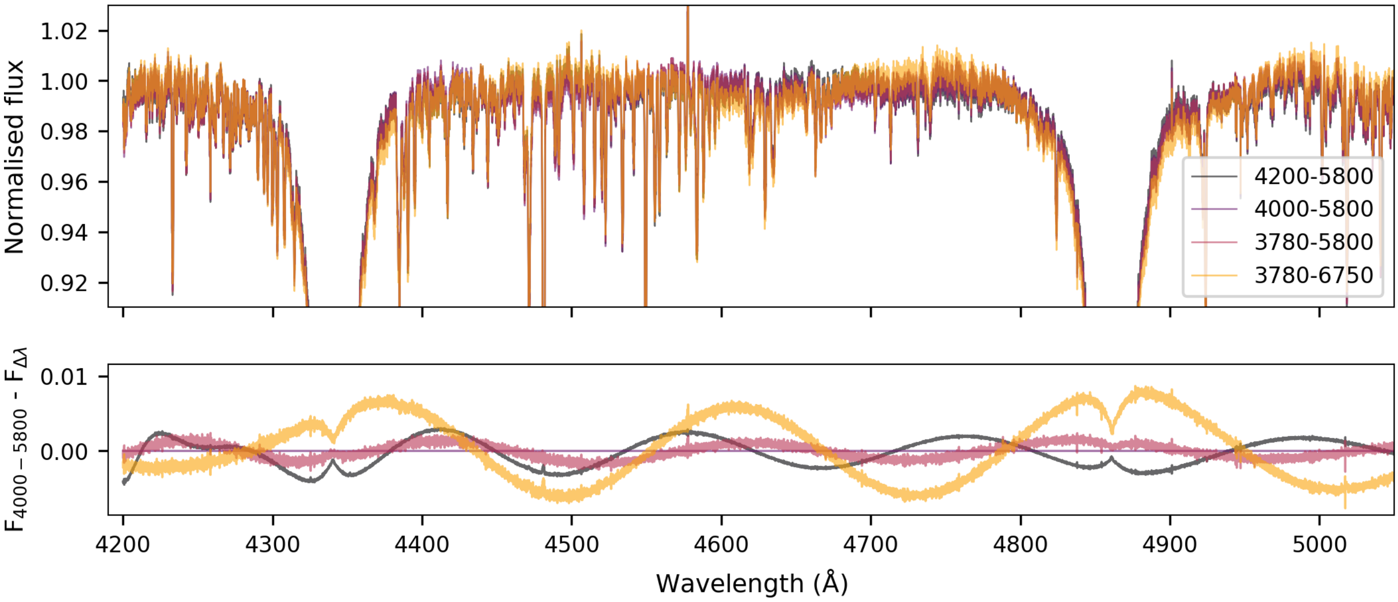

Fig. 5: Comparison of the normalisation quality when different wavelength regions are analysed. *Top panel:* spectra computed in the 4200-5800 Å (black), 4000-5800 Å (purple), 3780-5800 Å (red), 3780-6750 Å (yellow) wavelength regions are shown. *Bottom panel* shows the differences between the spectrum computed in the 4000-5800 Å range and those computed in the other wavelength regions as indicated by the same colours as in the top panel.

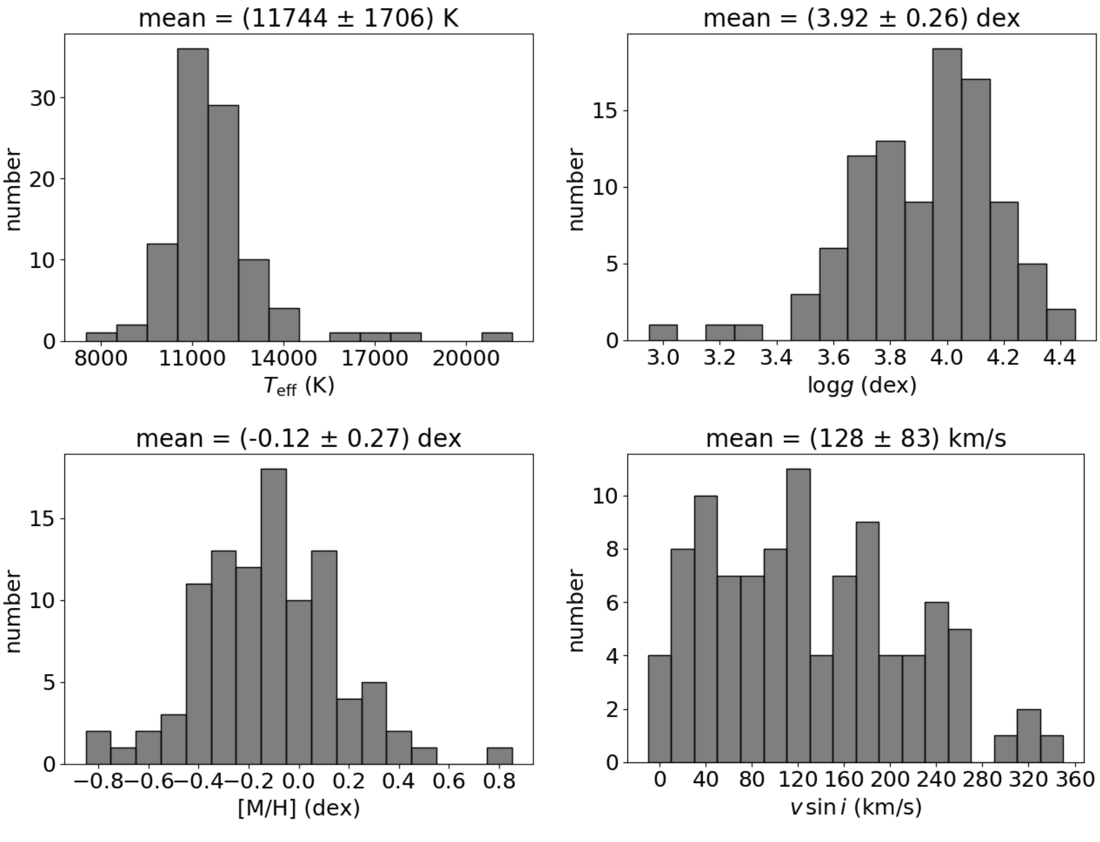

Fig. 6: Distributions of $T_{\rm eff}$, $\log g$, [M/H] and $v \sin i$.

- SPB: slowly pulsating B star (i.e. predominantly g-mode pulsations);
- const: constant star (i.e. no significant variability);
- EB: eclipsing binary;
- EV: ellipsoidal variable;
- β Cep: early-B star (i.e. predominantly p-mode pulsations);
- δ Sct: A- and early-F star with p- and g-mode pulsations;
- SLF: stochastic low-frequency variability;

Stars for which the variability type is also assigned a question mark (?) have a tentative classification. Also, in some cases, the inferred effective temperatures and surface gravities from our spectroscopic analysis were used to separate, for example, δ Sct and β Cep pulsators, which can have similar amplitude spectra.

We show the TESS light curves and amplitude spectra of four example stars in Fig. 7 to demonstrate the power of including TESS light curves in our analysis. First, is the SPB star HD 33599 (TIC 55295028), which has the typical signatures of multi-periodic g modes appearing in distinct groups in its amplitude spectrum (Kurtz et al. 2015; Van Beeck et al. 2021). Its light curve also has signatures of outbursts and hence it is a candidate pulsating Be star. We also note that we have identified HD 33599 as an SB2 system with many emission lines in its spectra, which makes it interesting to follow-up spectroscopically and understand the nature of its companion and evolutionary origin (see e.g. Shenar et al. 2020; Bodensteiner et al. 2020). Second, is the SPB / β Cep hybrid star HD 49193 (TIC 167523976), which has a low projected surface rotation rate, $v \sin i \simeq 40\,\mathrm{km\,s^{-1}}$, and an effective temperature of $T_{\rm eff} \simeq 21000$ K. It is the hottest star in our sample and is located close to the cool edge of the β Cep instability region. Third is the EB system AN Dor (TIC 220430912), which was recently re-visited by Southworth & Bowman (2022) to derive masses and radii from archival RVs and new TESS light curves. Fourth, is HD 40435 (TIC 31313111) which has the characteristic double-wave light curve and harmonic-series in its amplitude spectrum typical of rotation modulation (see e.g. Bowman et al. 2018). We identified LPV in this star's spectra that is likely associated with a CP2 nature.

As a vast improvement over previous studies that utilised short TESS light curves, our re-classification has the major advantage of improved frequency resolution from long-term TESS light curves. Similar to previous work, we find a high variability fraction (> 90%) in the TESS light curves of our sample. As mentioned previously, we do not extract pulsation, binary or rotation frequencies for follow-up modelling, as such an endeavour requires custom light curves and is the subject of future work. Our work has allowed to rank the most promising stars with reliable spectroscopy and clear signatures of binarity and/or pulsations to follow-up with detailed seismic modelling.

6. Discussion

6.1. Internal uncertainty trends

Apart from the total internal uncertainties discussed in Sect. 4.3, we also computed the internal uncertainties for the noiseless spectra in bins of $T_{\rm eff}$ and $v \sin i$. An overview of this can be found in Table 3 and is plotted in Fig. 8. One of the interesting features in this figure is the tail of high $T_{\rm eff}$ uncertainties in the ~ 9000 K regime. A closer look at the properties of spectra forming the tail reveals low metallicities and high projected rotational velocities which in turn implies apparent dearth of spectral lines of metals. This significant loss of information, where one has to rely exclusively on the Balmer lines to estimate the $T_{\rm eff}$-$\log g$ pair of parameters, results in larger uncertainties in $T_{\rm eff}$ and, to a lesser extent, $\log g$ of the star. We also note an increase in absolute uncertainties towards high $T_{\rm eff}$ values, yet relative uncertainties remain at the level of 2-3%, similar to the lower $T_{\rm eff}$ regime (see Table 3).

We also note scatter in $\log g$ for spectra with $T_{\rm eff} < 10\,000K$, i.e. for late A- and F-type stars. As discussed in Gebruers et al. (2021), the $\log g$ determination for these stars is degenerate with $T_{\rm eff}$, [M/H] and the continuum normalisation of the spectrum. Small offsets in the continuum result in large differences in $\log g$, which explains the larger internal uncertainty in this $T_{\rm eff}$ bin. The same trends in the internal uncertainties are reported by Straumit et al. (2022) for APOGEE (infrared) and BOSS (optical) spectra.

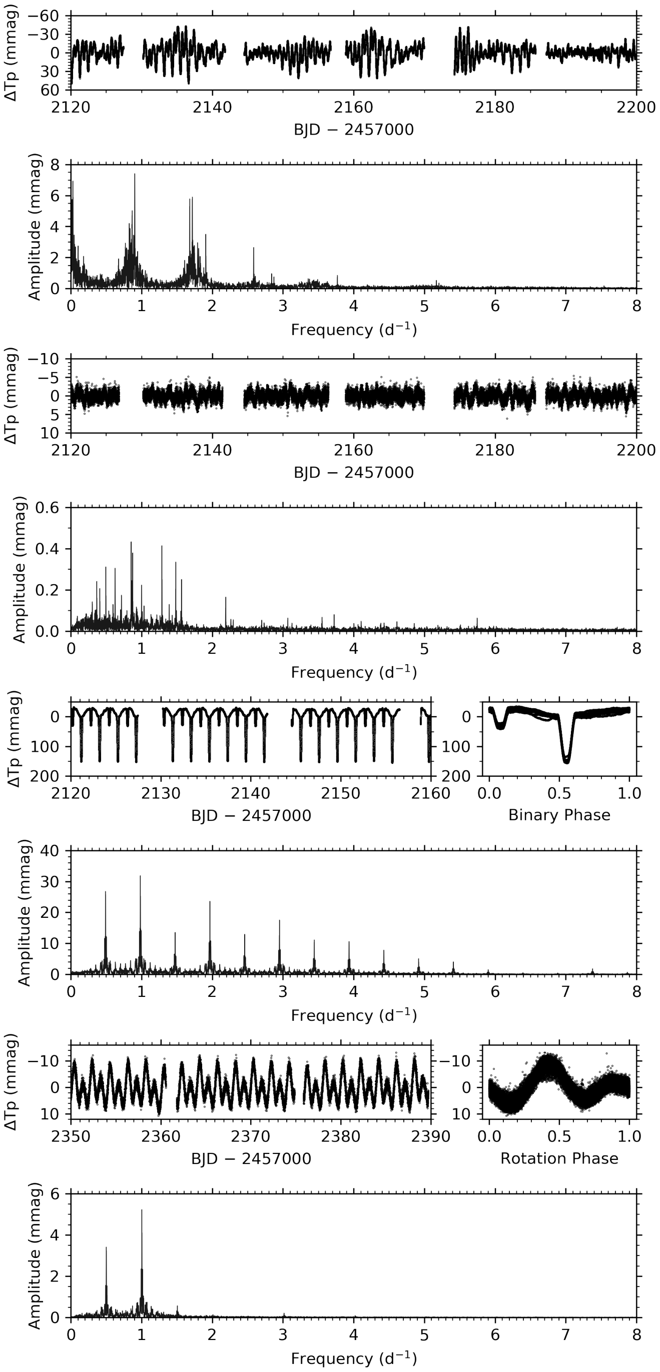

Fig. 7: Subsection of the 2-min TESS light curve and amplitude spectrum of four example stars. From top-to-bottom: TIC 55295028 (HD 33599; SPB), TIC 167523976 (HD 49193; SPB / β Cep), TIC 220430912 (AN Dor; EB), and TIC 31313111 (HD 40435; rot). For the latter two stars, a phase-folded light curve is shown in the top-right panel.

6.2. Newly discovered HgMn stars

Thirteen of the main sequence stars in our sample analysed with the ZETA-PAYNE were found to be new HgMn stars (or CP3 stars). These chemically peculiar (CP) stars, encountered among late-B

Table 3: Internal uncertainties for the surface parameters and the radial velocity in bins of $T_{\rm eff}$ and $v \sin i$ computed from a sample of 1000 simulated noiseless FEROS spectra.

Parameter	internal uncertainty									
	Bin 1	Bin 2	Bin 3	Bin 4	Bin 5	Bin 6	Bin 7	Bin 8	Bin 9	Bin 10
					as function of $T_{\rm eff}$					
Bin (kK)	6-7.9	7.9-9.8	9.8-11.7	11.7-13.6	13.6-15.5	15.5-17.4	17.4-19.3	19.3-21.2	21.2-23.1	23.1-25
$T_{\rm eff}$ (K)	211 (3%)	321 (4%)	226 (2%)	161 (1%)	267 (2%)	334 (2%)	438 (2%)	515 (3%)	597 (3%)	679 (3%)
log g (dex)	0.29	0.17	0.10	0.05	0.05	0.05	0.06	0.07	0.08	0.10
v sin i (km s^{-1})	11	18	14	10	11	10	10	9	9	12
ξ (km s^{-1})	1.3	1.9	2.1	1.9	2.1	2.0	2.3	2.2	2.1	3.3
[M/H] (dex)	0.19	0.18	0.15	0.11	0.10	0.09	0.10	0.11	0.11	0.12
RV (km s^{-1})	2.1	1.3	0.5	0.3	0.3	0.4	0.5	1.0	1.1	1.0
					as function of v sin i					
Bin (km s^{-1})	0-40	40-80	80-120	120-160	160-200	200-240	240-280	280-320	320-360	360-400
$T_{\rm eff}$ (K)	509	374	433	315	380	402	378	479	434	418
log g (dex)	0.09	0.08	0.10	0.10	0.09	0.11	0.13	0.17	0.13	0.16
v sin i (km s^{-1})	8	9	9	10	10	9	12	12	11	15
ξ (km s^{-1})	2.5	2.7	2.0	1.8	1.9	2.0	1.7	2.0	2.3	2.6
[M/H] (dex)	0.09	0.10	0.10	0.09	0.11	0.11	0.11	0.21	0.14	0.15
RV (km s^{-1})	0.2	0.4	0.5	1.0	0.4	0.5	0.7	1.8	1.1	1.6

types, have enhanced abundances of Hg and Mn (and other elements such as Ga, Sr and Y, Smith 1996). We optimised the Hg and Mn abundances of the 13 stars to confirm their CP3 classification. The wavelength range has been extended to 3930 Å in the blue part of the spectrum to include the HgII 3984 Å spectral line. The differences between the observed and the model spectra around the Hg and Mn lines disappear when the abundances of these elements are optimised in the models (left versus right panels of Figs. 9 and 10). For some stars there are still some features present in the residuals after optimising for Hg and Mn. This is probably caused by overabundances of other elements such as Y, but a detailed abundance analysis is beyond the scope of this paper.

HgMn stars are slow rotators with $< v \sin i >\sim 29\,{\rm km\,s^{-1}}$ (Abt et al. 1972) and have a high binarity rate with spectroscopic binarity percentages between 50-91 % (e.g. Hubrig & Mathys 1995; Schöller et al. 2010). About half of the binaries are found in SB2 systems, mostly with short orbital periods. Although they are thought to be non-magnetic CP stars, they show rotational modulation consistent with spots of overabundant chemical elements on the surface (e.g. Korhonen et al. 2013; Kochukhov et al. 2021). In CP2 (i.e. the ApBp stars) these spots can be explained by the presence of a magnetic field, but in HgMn stars the origin is not yet fully understood. Possible explanations are atomic diffusion processes in the outer stellar layers (Alecian et al. 2011) or maybe weak magnetic fields (Hubrig et al. 2020). Another cause for the variability seen in HgMn stars, aside from rotational modulation, are pulsations but not many pulsating HgMn stars have been detected yet (e.g. Alecian et al. 2009; Kochukhov et al. 2021).

From the TESS light curves we find that all 13 HgMn stars exhibit rotational modulation and none of them are pulsators. For a few targets also line profile variability is found in the spectra (this is indicated in column 4 of Table 6). Interestingly, only one of them is found in a SB1 binary: HD 44247. This would result in a binarity rate of only 8% (without correcting for observational biases) as opposed to what is found in other studies. Our observational biases include but are not limited to: (i) intentional bias against binary stars at the very early stage of the sample selection, (ii) exclusion of all stars that were nevertheless identified as SB2 binary systems in our sample prior to its detailed spectroscopic analysis based on the obtained FEROS spectra, and (iii) our ability to detect (especially long-period) binaries is limited by the number of acquired epochs (two in most cases), separation of some two months between them, and S/N in the obtained individual epoch spectra. Therefore, the above-quoted observed binary rate among HgMn stars in our sample should be taken with a big grain of salt.

None of these 13 stars have been classified as HgMn stars before, but μ Men was found to have an overabundance of Si (Houk & Cowley 1975) and CPD-60 944A has been classified as an α^2 CVn star with Si overabundance by Bernhard et al. (2015).

6.3. Spectroscopic Hertzsprung-Russell diagram

The stars from Table 6 are plotted in a spectroscopic Hertzsprung-Russell diagram (sHRD) in Fig. 11 in which the ordinate axis is defined as $\log{(T_{\rm eff}^4/g)}$. In the top panel, the stars are colour-coded following their spectroscopic classification, while on the bottom the symbols represent different photometric variability classes. Typical errors are shown, both for the uncertainties obtained from the ZETA-PAYNE and when the internal uncertainties are taken into account. We used the non-rotating MESA evolutionary tracks for solar metallicity and an exponential core overshoot of $f_{\rm ov}$ = 0.02, and the g-mode instability region from Burssens et al. (2020) to situate the stars in the sHRD. Most stars are intermediate-mass stars on the main sequence with masses around 2.5-4 $M_\odot$. There are however two to six stars, depending on which errors are taken into account, that seem to have evolved beyond the end of the main sequence.

We also include Fig. 12 which shows the same stars in the HRD, with luminosities calculated based on their *Gaia* G-band magnitudes, *Gaia* eDR3 photogeometric distances from Bailer-Jones et al. (2021), reddening values from the SFD dustmap (Schlafly & Finkbeiner 2011) and bolometric corrections calculated with the prescriptions from Pedersen et al. (2020). Apart from the g-mode instability region from Burssens et al. (2020) we also plotted the blue edge of the δ Sct instability strip from Dupret et al. (2005). Most of the stars classified as SPB(?) lie within the SPB instability strip. A large part of the sample is located outside of the SPB and δ Sct instability regions. This includes constant stars and stars with rotational modulation, but also 10 pulsators. We have also added to Fig. 12 stars from the recent work by Sharma et al. (2022). These authors studied pul-

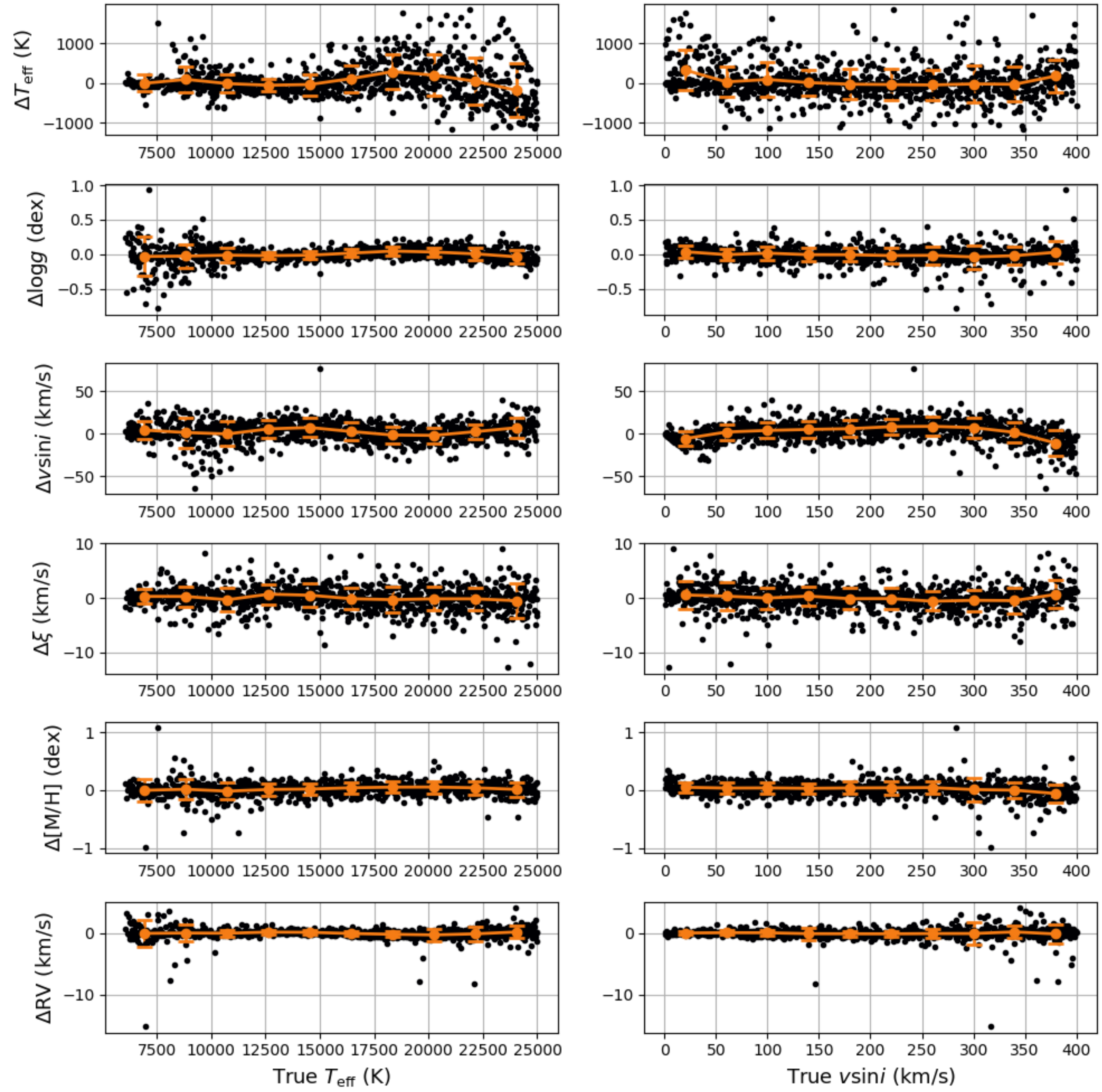

Fig. 8: Internal uncertainties (the difference between parameters predicted with the ZETA-PAYNE and the true values) for 1000 synthetic noiseless FEROS spectra are shown as a function of $T_{\rm eff}$ (*left*) and $v \sin i$ (*right*). The orange dots are the average uncertainties with standard deviation in bins of $T_{\rm eff}$ and $v \sin i$.

sating B-type stars in the Scorpio-Centaurus association using TESS light curves and also found pulsators below the SPB instability strip. Low-frequency pulsations in B-type stars cooler than the red edge of the SPB instability region have been noticed before. Salmon et al. (2014) claimed that these are fast rotating SPB stars that are seen equator-on and due to gravity darkening they appear cooler and fainter than if they would be observed pole-on. A similar explanation is given for high-frequency pulsators found in the literature between the red edge of the β Cep instability strip and the blue edge of the δ Sct instability strip, although it is also possible that these are binaries or misclassified stars that are actually variable due to rotational modulation (Balona et al. 2015, 2016).

In our sample there are eight stars classified as SPB that are situated below the SPB instability strip and that have g-mode frequencies higher than normally expected for these stars. These stars are HD 45835, θ Ret A, κ Men, HD 49531, μ Pic, HD 47478, 29 Dor, and HD 37027, and none of them are spectroscopic binaries. μ Pic, 29 Dor and HD 37027 are known to be Be stars. We did not include the cores of the Balmer lines in the spectral analysis for Be stars since they are in emission. Therefore the $T_{\rm eff}$ value which is derived from the Balmer lines might be

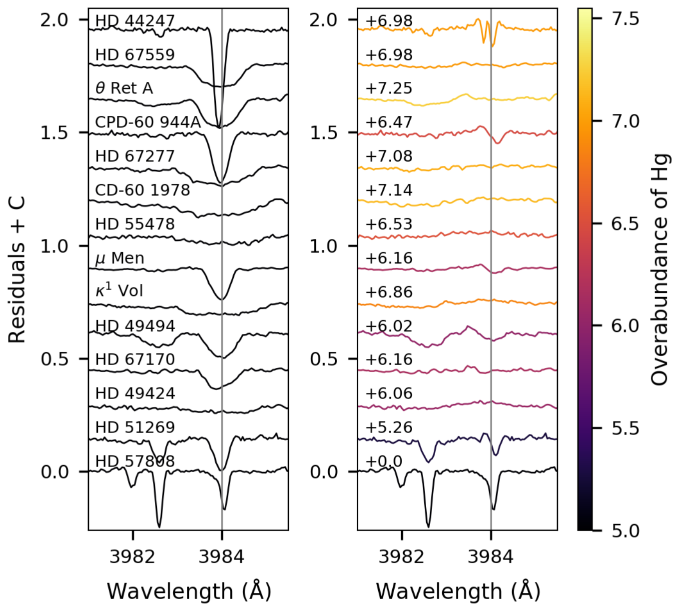

Fig. 9: Overabundance of Hg in HgMn stars. Left panel shows residuals around the HgII$_{3984}$ line between the observed spectrum and best-fitting GSSP spectrum with Hg abundance according to the metallicity of the star. Right panel shows the residuals when the Hg abundance is optimised for the star. The residuals in the right panel are colour-coded according to the Hg overabundance with respect to the abundance in the left panel. The value is also given for each star. The residuals of the different stars are offset with a constant value to plot all stars on the same figure.

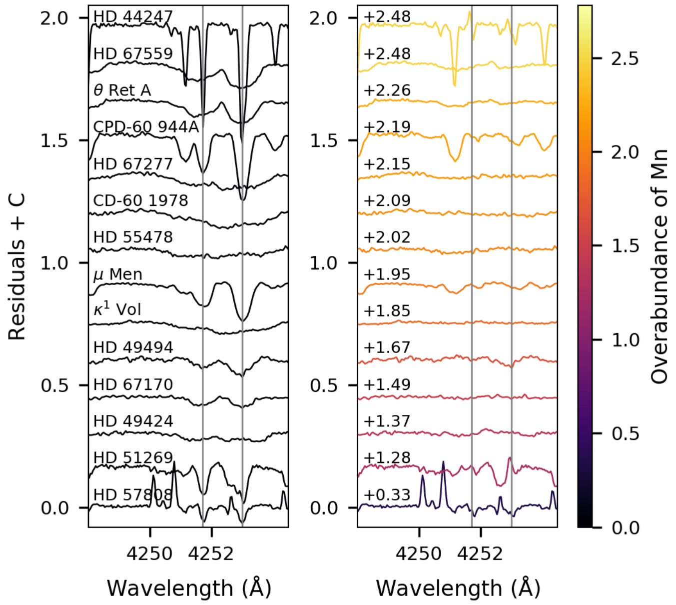

Fig. 10: Overabundance of Mn in HgMn stars. Similar as in Fig. 9 but for the MnII$_{4252}$ and MnII$_{4253}$ lines.

subject to large uncertainties. θ Ret A is a relatively slow rotator with $v \sin i$ equal to 44±13 km s^{-1}, but it situated relatively close to the red edge of the SPB instability strip. The other seven stars are rapid rotators and might thus be fast rotating SPB stars seen equator-on as explained by Salmon et al. (2014). Their high g-mode frequencies can be explained by fast rotation that has shifted their g-mode frequencies as observed in an inertial frame into a relatively high-frequency regime. Such an astrophysical interpretation has been proposed previously for bright SPB and Be stars observed from ground-based data (Aerts et al. 1999; De Cat & Aerts 2002; Aerts & Kolenberg 2005; Saesen et al. 2010, 2013; Mowlavi et al. 2013; Moździerski et al. 2014; Mowlavi et al. 2016; Moździerski et al. 2019), MOST space photometry (Walker et al. 2005; Aerts et al. 2006; Saio et al. 2007), CoRoT space photometry (Neiner et al. 2009; Diago et al. 2009), and *Kepler*/K2 space photometry (Pápics et al. 2017; White et al. 2017; Pedersen et al. 2021; Szewczuk et al. 2021). The major frequency shifts are indeed expected for prograde and retrograde sectoral modes in the gravito-inertial regime as induced by the Coriolis acceleration due to the fast rotation (Townsend 2005; Salmon et al. 2014; Saio et al. 2017; Aerts et al. 2019).

Because of the rapid rotation of these SPB stars evidenced by large v sin i values inferred from our FEROS spectroscopy, their apparently too low $T_{\rm eff}$ relative to the SPB instability region are likely to be due to the gravity darkening phenomenon. This phenomenon results from the variation of $T_{\rm eff}$ with local gravity on the surface of a non-spherical star (von Zeipel 1924) and therefore implies a lower $T_{\rm eff}$ at the equator than at the pole of a rapidly rotating star. As is recently demonstrated in Fabry et al. (2022, and private communication), the variation of $T_{\rm eff}$ of a typical rapidly rotating B-type star amounts to about 5% in the course of its main-sequence evolution. This $T_{\rm eff}$ variation from stellar pole to equator can explain the apparent temperature offset from the red edge of the SPB instability strip in the HRD for all but three stars. The stars for which gravity darkening is not sufficient to place them within the SPB instability strip are two Be stars HD 37027 and 29 Dor, and the star HD 47478. However, the 5% $T_{\rm eff}$ difference derived in Fabry et al. (2022) is based on MESA models which is limited to 1D approximations. A 2D study with the ESTER code (Bouchaud et al. 2020) has shown that for the A7-type star Altair the temperature difference between equator and pole amounts to approximately 2000 K. Thus 5% is only a lower limit and gravity darkening effects can be higher when the proper 2D structure of fast rotators is taken into account instead of 1D approximations.

We also find four seemingly p-mode pulsators (i.e. identified as δ Sct stars based on their TESS light curves exhibiting pulsation frequencies above ∼ 4 d^{-1}) in between the β Cep and δ Sct instability regions (HD 44533, HD 55478, HD 67420, and η Phe). These 4 stars are all fast rotators, and HD 44533 and η Phe are Be stars. They are probably misclassified as δ Sct stars, just as the high-frequency mode near ∼ 4 d^{-1} of the rapidly rotating SPB pulsator HD 43317 was initially thought to be a p mode (Pápics et al. 2012) while it actually concerns a rotationally shifted retrograde quadrupole mode (Buysschaert et al. 2018). In the case of the Be stars, their derived surface parameters are uncertain due to their fast rotation and circumstellar disk.

6.4. Multiple linear regression

We looked for correlations between all five spectroscopic parameters and the luminosity via backward multiple linear regression. This was done by taking one of these six parameters as the dependent variable and performing a multiple linear regression with the other five parameters as independent variables. We computed the coefficient of determination (R^2) to determine how well the set of independent variables could predict the dependent variable, where R^2 = 1 would mean a perfect fit. For each of the independent variables we then checked if they were significant in this relation by doing a t-test. If the p-value from this t-test was

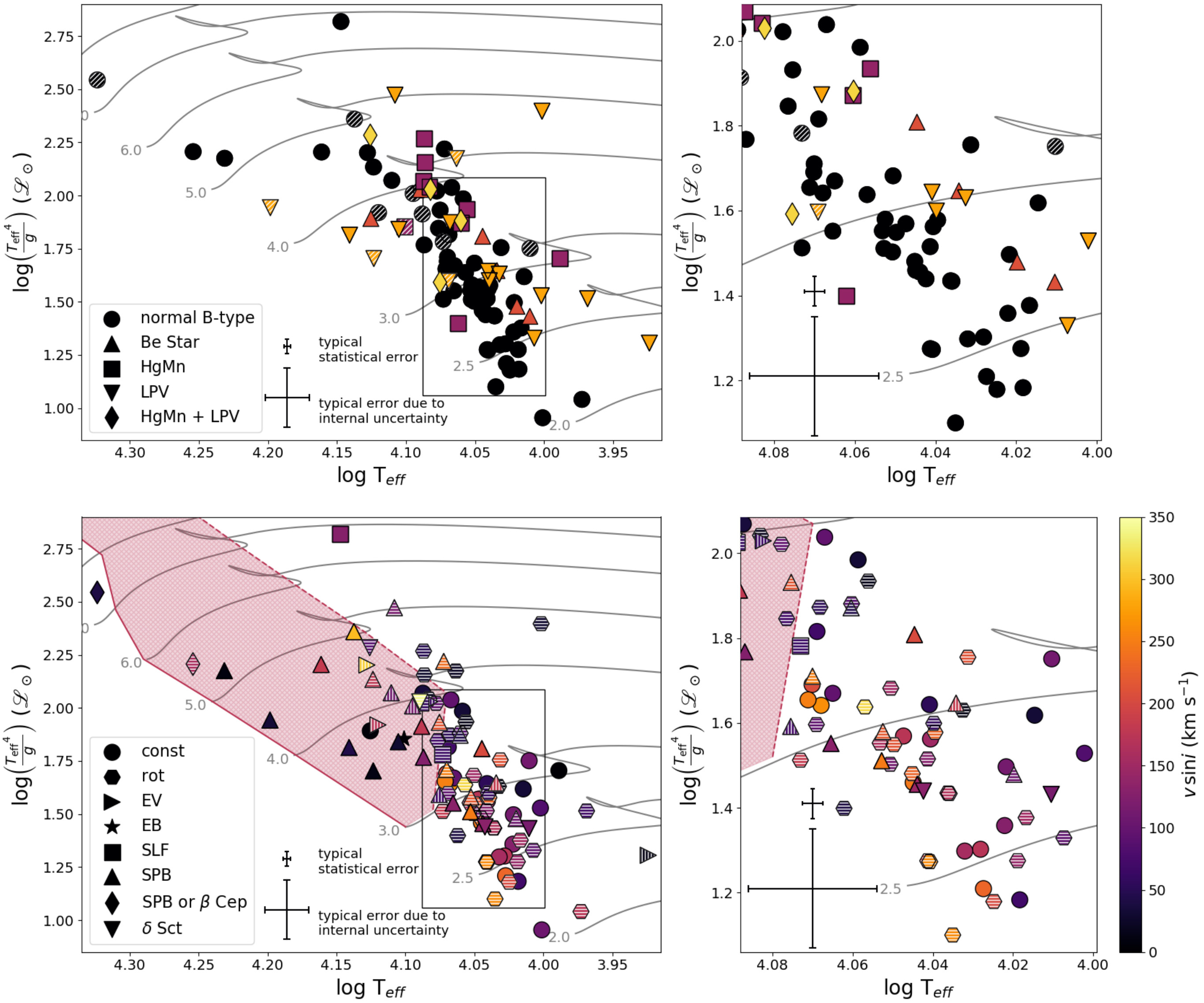

Fig. 11: sHRD containing all stars from Table 6. *Top:* the stars are colour-coded according to their spectroscopic information. The hatched symbols are SB1 binaries. *Bottom:* same as top panel, but now the photometric variability is indicated by different symbols. They are colour-coded according to their $v\sin i$ values. Stars with dominant rotational variability are hatched with white horizontal lines and symbols hatched with white vertical lines are stars that can either have variability according to the symbol or rotational variability. The right panels are a zoom in of the region below the SPB instability strip. Typical errors are plotted, both the statistical error returned by the ZETA-PAYNE as the ones including the internal uncertainties. Non-rotating MESA evolutionary tracks (in grey) and the g-mode instability strip (red shaded area) from Burssens et al. (2020) are shown as well.

above 0.05 the variable was assumed insignificant. The multiple linear regression was then repeated in the same way but without the least significant variable until only significant variables remained. The relations we found from this analysis are given in Table 4.

In the first three models $\log L$, $T_{\rm eff}$, $\log g$ and [M/H] are related to each other. These are well-known relations expected from standard stellar structure and evolution theory. The fourth relation links ξ to $\log L$, $T_{\rm eff}$, $v\sin i$ and [M/H]. It suggests a decrease of the microturbulent velocity with increasing luminosity within our sample. This is in contradiction with the expectation of turbulent velocity fields getting larger as the surface gravity (luminosity) of star decreases (increases) (e.g., Gray 2005). This latter interpretation is supported by observational studies of single stars (e.g., Hunter et al. 2008) and binary systems (e.g., Tkachenko et al. 2014), as well as by theoretical studies of sub-surface convective zones in intermediate- and high-mass stars (e.g., Cantiello et al. 2009). We currently do not have a good physical interpretation of the (weak) opposite trend we found but we speculate it may have a methodological explanation in that the microturbulent velocity in B-type stars cannot be reliably inferred from the global fitting procedure of their entire optical spectra. Instead, one might need to focus on a detailed analysis of carefully selected spectral lines that are sensitive to ξ, such as the Si III triplet at 4552 Å, 4567 Å, and 4574 Å and/or He I lines in the optical part of the spectrum. This is different from cooler stars with many metal lines for which ξ can be determined from the entire spectrum since ξ values from all element lines, including possible wrong values from lines that are less sensitive to ξ, are averaged out.

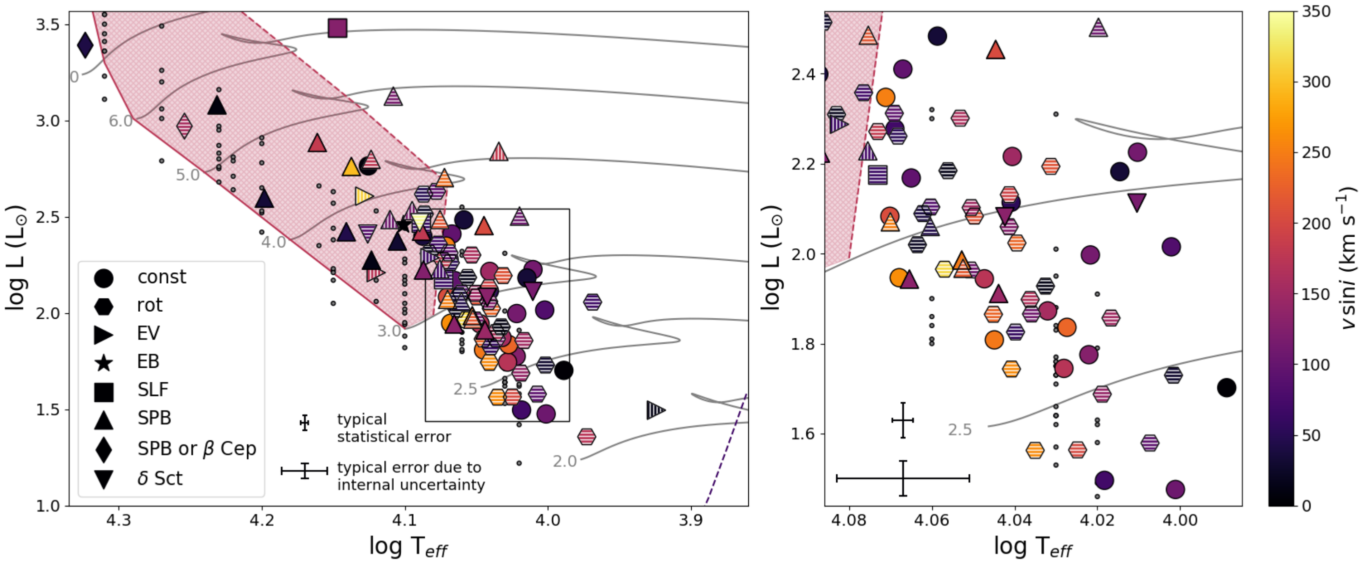

Fig. 12: HRD. Same figure as the bottom panel of Fig. 11 but with luminosity on the y-axis. The small grey dots are B-type stars in the Scorpio-Centaurus association from Sharma et al. (2022). Non-rotating MESA evolutionary tracks from Burssens et al. (2020) are shown in grey, and the red shaded area is the g-mode instability strip from Burssens et al. (2020). The purple dashed line is the blue edge of the δ Sct instability strip from Dupret et al. (2005).

Table 4: Multiple linear regression results

Predictors	Estimate	p-value	R^2
Dependent variable log L			
Intercept	0.40 ± 0.04	...	0.751
$T_{\rm eff}$	1.05 ± 0.07	< 0.001	
log g	-0.44 ± 0.06	< 0.001	
Dependent variable $T_{\rm eff}$			
Intercept	-0.18 ± 0.04	...	0.691
log L	0.66 ± 0.05	< 0.001	
log g	0.28 ± 0.05	< 0.001	
Dependent variable log g			
Intercept	0.85 ± 0.05	...	0.445
log L	-0.89 ± 0.11	< 0.001	
$T_{\rm eff}$	0.87 ± 0.16	< 0.001	
[M/H]	-0.20 ± 0.08	0.015	
Dependent variable ξ			
Intercept	0.29 ± 0.06	...	0.463
log L	-0.29 ± 0.11	0.01	
$T_{\rm eff}$	0.32 ± 0.16	0.043	
$v \sin i$	0.26 ± 0.06	< 0.001	
[M/H]	-0.41 ± 0.09	< 0.001	

7. Conclusions

We have analysed high-resolution FEROS spectra of a sample of 166 variable stars identified using TESS space photometry. Our follow-up spectroscopic data has been reduced with the CERES pipeline, to which we added four new capabilities in order to obtain smooth reduced normalised spectra without artificial features and cosmic hits.

We have determined surface parameters with the ZETA-PAYNE framework for all Galactic single stars and SB1 systems in the sample, excluding SB2 systems and supergiants in the LMC galaxy. Apart from the uncertainties deduced with the ZETA-PAYNE, the internal uncertainties inherent to the neural network and fitting approach were also taken into account. It was shown that, within the internal uncertainties, the parameters are not affected by the wavelength region that is analysed. If the neural network used in this paper is applied to longer wavelength regions, the number of coefficients for the Chebyshev polynomial representing the response function should be optimised for the respective wavelength range. Overall, in the considered wavelength interval from 4000 Å to 5800 Å and with 25 Chebyshev coefficients representing the residual response function of the instrument, the estimated internal uncertainties amount to some 3% and 5% in $T_{\rm eff}$ and $v \sin i$, respectively, and 0.1 dex in [M/H] and log g.

We have found that 13 of the stars in the sample are chemically peculiar HgMn stars. The best-fitting spectra returned by the ZETA-PAYNE framework do not fit well the observed spectra of these stars, specifically in spectral windows that contain lines of Hg, Mn, Y, and some other chemical elements. Our ad-hoc abundance analysis of several chemical elements in the spectra of these HgMn stars with the GSSP software package revealed strong overabundances, confirming peculiar nature of the stars.

The spectroscopic values and luminosities computed from *Gaia* eDR3 data were used to place the stars in a spectroscopic and classical HRD. In these diagrams, eight stars classified as SPB with relatively high g-mode frequencies are located below the (non-rotating) SPB instability region. In all cases the location and variability of these stars can plausibly be explained by their fast rotation, which is expected to significantly affect the instability regions of early-type stars (see Szewczuk & Daszyńska-Daszkiewicz 2017) and shift their observed g-mode frequencies into the high-frequency regime. Therefore, we conclude to have found spectroscopic evidence of a group of fast rotating g-mode B-type pulsators monitored by TESS, covering the area between the SPB instability strip and the blue edge of the δ Sct strip. For all but three stars, the lower temperatures relative to the SPB instability strip obtained for these stars could be related to the gravity darkening effect. Due to their rapid rotation the observed temperature at the equator is ~5% lower than the temperature at the poles (Fabry et al. 2022).

The multiple linear regression analysis involving five spectroscopic parameters and stellar luminosity revealed well-known relations between $\log L$, T_{eff}, $\log g$ and [M/H] of the star as predicted by stellar evolution theory. A somewhat unexpected result is the weak negative relation found between $\log L$ and ξ which we attribute to our methodology of inferring ξ from the entire optical spectrum instead of selecting specific lines sensitive to ξ.

Our spectrum fitting approach with the current neural network trained on LTE GSSP models is not suitable for the analysis of the spectra of supergiants. This will only be possible when NLTE models with possibility to include physics of stellar winds are used to train the neural network. Similarly, it is not yet possible to analyse SB2 systems with this version of the ZETA-PAYNE since this requires the analysis of either their composite or disentangled spectra. Analysis of the composite spectra of SB2 binaries is challenging and typically associated with large uncertainties in the inferred atmospheric parameters of both binary components (see, e.g., Tkachenko 2015). On the other hand, analysis of the disentangled spectra is as precise as spectrum analysis of spectra of single stars, provided a uniform orbital phase coverage is achieved for the SB2 system in consideration (see, e.g., Hadrava 1995; Ilijic et al. 2004). Therefore, detailed analysis of the spectra of evolved supergiants and of SB2 binary systems requires a dedicated effort and is beyond the scope of this paper.

Acknowledgements. The research leading to these results has (partially) received funding from the KU Leuven Research Council (grant C16/18/005: PARADISE), from the Research Foundation Flanders (FWO) under grant agreement G0H5416N (ERC Runner Up Project), as well as from the BELgian federal Science Policy Office (BELSPO) through PRODEX grant PLATO. SG, LIJ, TVR, and DMB gratefully acknowledge support from the Research Foundation Flanders (FWO) by means of PhD Aspirant mandates, and Junior and Senior Postdoctoral Fellowships, under contracts No. 11E5620N, No. 1124321N, No. 12ZB620N, and No. 1286521N, respectively. LM thanks the European Space Agency (ESA) and the Belgian Federal Science Policy Office (BELSPO) for their support in the framework of the PRODEX MAESTRO Programme. The computational resources and services used in this work were provided by the VSC (Flemish Supercomputer Centre), funded by the Research Foundation - Flanders (FWO) and the Flemish Government. This research has made use of the SIMBAD database, operated at CDS, Strasbourg, France; the SAO/NASA Astrophysics Data System; and the VizieR catalog access tool, CDS, Strasbourg, France. The TESS data presented in this paper were obtained from the Mikulski Archive for Space Telescopes (MAST) at the Space Telescope Science Institute (STScI), which is operated by the Association of Universities for Research in Astronomy, Inc., under NASA contract NAS5-26555. Support to MAST for these data is provided by the NASA Office of Space Science via grant NAG5-7584 and by other grants and contracts. Funding for the TESS mission is provided by the NASA Explorer Program. Some of the observations used in this work were obtained with the FEROS spectrograph attached to the 2.2-m MPG/ESO telescope at the La Silla observatory under program 0104.A-9001(A). This work has made use of data from the European Space Agency (ESA) mission *Gaia* (`https://www.cosmos.esa.int/gaia`), processed by the *Gaia* Data Processing and Analysis Consortium (DPAC, `https://www.cosmos.esa.int/web/gaia/dpac/consortium`). Funding for the DPAC has been provided by national institutions, in particular the institutions participating in the *Gaia* Multilateral Agreement. This work made use of the python packages: NumPy (van der Walt et al. 2011), Astropy (Astropy Collaboration et al. 2013, 2018), SciPy (Virtanen et al. 2020), Matplotlib (Hunter 2007), pandas (Wes McKinney 2010), PyTorch (Paszke et al. 2019) and dustmaps (Green 2018).

References

Abt, H. A., Chaffee, F. H., & Suffolk, G. 1972, ApJ, 175, 779
Aerts, C. 2021, Reviews of Modern Physics, 93, 015001
Aerts, C., De Cat, P., Kuschnig, R., et al. 2006, ApJ, 642, L165
Aerts, C., De Cat, P., Peeters, E., et al. 1999, A&A, 343, 872
Aerts, C. & Kolenberg, K. 2005, A&A, 431, 615
Aerts, C., Mathis, S., & Rogers, T. M. 2019, ARA&A, 57, 35
Alecian, G., Gebran, M., Auvergne, M., et al. 2009, A&A, 506, 69
Alecian, G., Stift, M. J., & Dorfi, E. A. 2011, MNRAS, 418, 986
Angelou, G. C., Bellinger, E. P., Hekker, S., et al. 2020, MNRAS, 493, 4987
Astropy Collaboration, Price-Whelan, A. M., Sipőcz, B. M., et al. 2018, AJ, 156, 123
Astropy Collaboration, Robitaille, T. P., Tollerud, E. J., et al. 2013, A&A, 558, A33
Auvergne, M., Bodin, P., Boisnard, L., et al. 2009, A&A, 506, 411
Bailer-Jones, C. A. L., Rybizki, J., Fouesneau, M., Demleitner, M., & Andrae, R. 2021, AJ, 161, 147
Balona, L. A., Baran, A. S., Daszyńska-Daszkiewicz, J., & De Cat, P. 2015, MNRAS, 451, 1445
Balona, L. A., Engelbrecht, C. A., Joshi, Y. C., et al. 2016, MNRAS, 460, 1318
Balona, L. A., Pigulski, A., De Cat, P., et al. 2011, MNRAS, 413, 2403
Bernhard, K., Hümmerich, S., Otero, S., & Paunzen, E. 2015, A&A, 581, A138
Bodensteiner, J., Shenar, T., Mahy, L., et al. 2020, A&A, 641, A43
Borucki, W. J., Koch, D., Basri, G., et al. 2010, Science, 327, 977
Bouchaud, K., Domiciano de Souza, A., Rieutord, M., Reese, D. R., & Kervella, P. 2020, A&A, 633, A78
Bowman, D. M. 2020, Frontiers in Astronomy and Space Sciences, 7, 70
Bowman, D. M., Aerts, C., Johnston, C., et al. 2019a, A&A, 621, A135
Bowman, D. M., Burssens, S., Pedersen, M. G., et al. 2019b, Nature Astronomy, 3, 760
Bowman, D. M., Burssens, S., Simón-Díaz, S., et al. 2020, A&A, 640, A36
Bowman, D. M., Buysschaert, B., Neiner, C., et al. 2018, A&A, 616, A77
Brahm, R., Jordán, A., & Espinoza, N. 2017, PASP, 129, 034002
Bruntt, H., Basu, S., Smalley, B., et al. 2012, MNRAS, 423, 122
Burssens, S., Bowman, D. M., Aerts, C., et al. 2019, MNRAS, 489, 1304
Burssens, S., Simón-Díaz, S., Bowman, D. M., et al. 2020, A&A, 639, A81
Buysschaert, B., Aerts, C., Bowman, D. M., et al. 2018, A&A, 616, A148
Cantiello, M., Langer, N., Brott, I., et al. 2009, A&A, 499, 279
Christensen-Dalsgaard, J. 2002, Reviews of Modern Physics, 74, 1073
De Cat, P. & Aerts, C. 2002, A&A, 393, 965
Diago, P. D., Gutiérrez-Soto, J., Auvergne, M., et al. 2009, A&A, 506, 125
Donati, J. F., Semel, M., Carter, B. D., Rees, D. E., & Collier Cameron, A. 1997, MNRAS, 291, 658
Dupret, M. A., Grigahcène, A., Garrido, R., Gabriel, M., & Scuflaire, R. 2005, A&A, 435, 927
Ekström, S., Georgy, C., Eggenberger, P., et al. 2012, A&A, 537, A146
Fabry, M., Marchant, P., & Sana, H. 2022, arXiv e-prints, arXiv:2202.08852
Gebruers, S., Straumit, I., Tkachenko, A., et al. 2021, A&A, 650, A151
Gray, D. F. 2005, The Observation and Analysis of Stellar Photospheres
Green, G. 2018, The Journal of Open Source Software, 3, 695
Hadrava, P. 1995, A&AS, 114, 393
Houk, N. & Cowley, A. P. 1975, University of Michigan Catalogue of two-dimensional spectral types for the HD stars. Volume I. Declinations -90_ to -53_*f*0.
Hubrig, S., Järvinen, S. P., Korhonen, H., et al. 2020, MNRAS, 495, L97
Hubrig, S. & Mathys, G. 1995, Comments on Astrophysics, 18, 167
Hunter, I., Lennon, D. J., Dufton, P. L., et al. 2008, A&A, 479, 541
Hunter, J. D. 2007, Computing in Science Engineering, 9, 90
Ilijic, S., Hensberge, H., Pavlovski, K., & Freyhammer, L. M. 2004, in Astronomical Society of the Pacific Conference Series, Vol. 318, Spectroscopically and Spatially Resolving the Components of the Close Binary Stars, ed. R. W. Hilditch, H. Hensberge, & K. Pavlovski, 111–113
Jenkins, J. M., Twicken, J. D., McCauliff, S., et al. 2016, in Proc. SPIE, Vol. 9913, Software and Cyberinfrastructure for Astronomy IV, 99133E
Johnston, C., Tkachenko, A., Aerts, C., et al. 2019, MNRAS, 482, 1231
Kaufer, A., Stahl, O., Tubbesing, S., et al. 1999, The Messenger, 95, 8
Kochukhov, O., Khalack, V., Kobzar, O., et al. 2021, MNRAS, 506, 5328
Korhonen, H., González, J. F., Briquet, M., et al. 2013, A&A, 553, A27
Kupka, F., Piskunov, N., Ryabchikova, T. A., Stempels, H. C., & Weiss, W. W. 1999, A&AS, 138, 119
Kurtz, D. W. 1985, MNRAS, 213, 773
Kurtz, D. W., Shibahashi, H., Murphy, S. J., Bedding, T. R., & Bowman, D. M. 2015, MNRAS, 450, 3015
Langer, N. 2012, ARA&A, 50, 107
Langer, N. & Kudritzki, R. P. 2014, A&A, 564, A52
Lehmann, H., Tkachenko, A., Semaan, T., et al. 2011, A&A, 526, A124
Maeder, A. & Meynet, G. 2000, ARA&A, 38, 143
Michielsen, M., Pedersen, M. G., Augustson, K. C., Mathis, S., & Aerts, C. 2019, A&A, 628, A76
Miglio, A., Montalbán, J., Noels, A., & Eggenberger, P. 2008, MNRAS, 386, 1487
Mombarg, J. S. G., Dotter, A., Van Reeth, T., et al. 2020, ApJ, 895, 51
Mombarg, J. S. G., Van Reeth, T., Pedersen, M. G., et al. 2019, MNRAS, 485, 3248
Moravveji, E., Aerts, C., Pápics, P. I., Triana, S. A., & Vandoren, B. 2015, A&A, 580, A27
Moravveji, E., Townsend, R. H. D., Aerts, C., & Mathis, S. 2016, ApJ, 823, 130
Mowlavi, N., Barblan, F., Saesen, S., & Eyer, L. 2013, A&A, 554, A108
Mowlavi, N., Saesen, S., Semaan, T., et al. 2016, A&A, 595, L1
Moździerski, D., Pigulski, A., Kołaczkowski, Z., et al. 2019, A&A, 632, A95

Moździerski, D., Pigulski, A., Kopacki, G., Kołaczkowski, Z., & Stęślicki, M. 2014, Acta Astron., 64, 89
Neiner, C., Gutiérrez-Soto, J., Baudin, F., et al. 2009, A&A, 506, 143
Niemczura, E., Murphy, S. J., Smalley, B., et al. 2015, MNRAS, 450, 2764
Niemczura, E., Polińska, M., Murphy, S. J., et al. 2017, MNRAS, 470, 2870
Pápics, P. I., Briquet, M., Baglin, A., et al. 2012, A&A, 542, A55
Pápics, P. I., Tkachenko, A., Van Reeth, T., et al. 2017, A&A, 598, A74
Paszke, A., Gross, S., Massa, F., et al. 2019, in Advances in Neural Information Processing Systems 32 (Curran Associates, Inc.), 8024–8035
Pedersen, M. G., Aerts, C., Pápics, P. I., et al. 2021, Nature Astronomy, 5, 715
Pedersen, M. G., Aerts, C., Pápics, P. I., & Rogers, T. M. 2018, A&A, 614, A128
Pedersen, M. G., Chowdhury, S., Johnston, C., et al. 2019, ApJ, 872, L9
Pedersen, M. G., Escorza, A., Pápics, P. I., & Aerts, C. 2020, MNRAS, 495, 2738
Pinsonneault, M. H., Elsworth, Y., Epstein, C., et al. 2014, ApJS, 215, 19
Raskin, G., van Winckel, H., Hensberge, H., et al. 2011, A&A, 526, A69
Ricker, G. R., Winn, J. N., Vanderspek, R., et al. 2015, Journal of Astronomical Telescopes, Instruments, and Systems, 1, 014003
Saesen, S., Briquet, M., Aerts, C., Miglio, A., & Carrier, F. 2013, AJ, 146, 102
Saesen, S., Carrier, F., Pigulski, A., et al. 2010, A&A, 515, A16
Saio, H., Cameron, C., Kuschnig, R., et al. 2007, ApJ, 654, 544
Saio, H., Ekström, S., Mowlavi, N., et al. 2017, MNRAS, 467, 3864
Salmon, S. J. A. J., Montalbán, J., Reese, D. R., Dupret, M. A., & Eggenberger, P. 2014, A&A, 569, A18
Schlafly, E. F. & Finkbeiner, D. P. 2011, ApJ, 737, 103
Schöller, M., Correia, S., Hubrig, S., & Ageorges, N. 2010, A&A, 522, A85
Sekaran, S., Tkachenko, A., Abdul-Masih, M., et al. 2020, A&A, 643, A162
Sekaran, S., Tkachenko, A., Johnston, C., & Aerts, C. 2021, A&A, 648, A91
Sharma, A. N., Bedding, T. R., Saio, H., & White, T. R. 2022, arXiv e-prints, arXiv:2203.02582
Shenar, T., Bodensteiner, J., Abdul-Masih, M., et al. 2020, A&A, 639, L6
Shulyak, D., Tsymbal, V., Ryabchikova, T., Stütz, C., & Weiss, W. W. 2004, A&A, 428, 993
Silva Aguirre, V., Casagrande, L., Basu, S., et al. 2012, ApJ, 757, 99
Smith, K. C. 1996, Ap&SS, 237, 77
Sobol, I. M. 1967, USSR Comp. Math. and Math. Phys., 7, 86
Southworth, J. & Bowman, D. M. 2022, arXiv e-prints, arXiv:2203.15365
Southworth, J., Bowman, D. M., & Pavlovski, K. 2021, MNRAS, 501, L65
Southworth, J., Bowman, D. M., Tkachenko, A., & Pavlovski, K. 2020, MNRAS, 497, L19
Stoehr, F., White, R., Smith, M., et al. 2008, in Astronomical Society of the Pacific Conference Series, Vol. 394, Astronomical Data Analysis Software and Systems XVII, ed. R. W. Argyle, P. S. Bunclark, & J. R. Lewis, 505
Straumit, I., Tkachenko, A., Gebruers, S., et al. 2022, arXiv e-prints, arXiv:2203.14538
Szewczuk, W. & Daszyńska-Daszkiewicz, J. 2015, MNRAS, 453, 277
Szewczuk, W. & Daszyńska-Daszkiewicz, J. 2017, MNRAS, 469, 13
Szewczuk, W. & Daszyńska-Daszkiewicz, J. 2018, MNRAS, 478, 2243
Szewczuk, W., Walczak, P., & Daszyńska-Daszkiewicz, J. 2021, MNRAS, 503, 5894
Szewczuk, W., Walczak, P., Daszyńska-Daszkiewicz, J., & Moździerski, D. 2022, MNRAS, 511, 1529
Thygesen, A. O., Frandsen, S., Bruntt, H., et al. 2012, A&A, 543, A160
Ting, Y.-S., Conroy, C., Rix, H.-W., & Cargile, P. 2019, ApJ, 879, 69
Tkachenko, A. 2015, A&A, 581, A129
Tkachenko, A., Aerts, C., Yakushechkin, A., et al. 2013a, A&A, 556, A52
Tkachenko, A., Degroote, P., Aerts, C., et al. 2014, MNRAS, 438, 3093
Tkachenko, A., Lehmann, H., Smalley, B., Debosscher, J., & Aerts, C. 2012, MNRAS, 422, 2960
Tkachenko, A., Lehmann, H., Smalley, B., & Uytterhoeven, K. 2013b, MNRAS, 431, 3685
Tkachenko, A., Pavlovski, K., Johnston, C., et al. 2020, A&A, 637, A60
Tkachenko, A., Van Reeth, T., Tsymbal, V., et al. 2013c, A&A, 560, A37
Townsend, R. H. D. 2005, MNRAS, 364, 573
Tsymbal, V. 1996, in Astronomical Society of the Pacific Conference Series, Vol. 108, M.A.S.S., Model Atmospheres and Spectrum Synthesis, ed. S. J. Adelman, F. Kupka, & W. W. Weiss, 198
Uytterhoeven, K., Moya, A., Grigahcène, A., et al. 2011, A&A, 534, A125
Van Beeck, J., Bowman, D. M., Pedersen, M. G., et al. 2021, A&A, 655, A59
van der Walt, S., Colbert, S. C., & Varoquaux, G. 2011, Computing in Science and Engineering, 13, 22
Van Reeth, T., Mombarg, J. S. G., Mathis, S., et al. 2018, A&A, 618, A24
Van Reeth, T., Tkachenko, A., Aerts, C., et al. 2015, ApJS, 218, 27
Virtanen, P., Gommers, R., Oliphant, T. E., et al. 2020, Nature Methods, 17, 261
von Zeipel, H. 1924, MNRAS, 84, 665
Walker, G. A. H., Kuschnig, R., Matthews, J. M., et al. 2005, ApJ, 635, L77
Wes McKinney. 2010, in Proceedings of the 9th Python in Science Conference, ed. Stéfan van der Walt & Jarrod Millman, 56 – 61
White, T. R., Pope, B. J. S., Antoci, V., et al. 2017, MNRAS, 471, 2882

Table 5: Photometric classification. Stars indicated with an ‘*’ are LMC members.

Name	TIC	TESS sectors	Photometry
Galactic single stars and SB1 systems			
29 Dor	277103567	2,4,5,27-35,37,38	rot? / SPB?
CD-601929	358467087	1,4,7-11,27,31,34-37	rot + SLF?
CD-601931	358466708	1,7-11,27,31,35-37	SPB
CD-601954	372913582	1,4,7-11,27,31,34-37	rot?
CD-601978	364398190	1,4,7-11,27,31,34-37	rot?
CPD-60944A	358467046	-	rot
CPD-60944B	358467046	-	rot
η Phe	281703960	1-2,28-29	δ Sct
HD 1256	419065817	2,29	EV? / rot?
HD 201108	115177591	1,28	SPB
HD 208495	355141264	1,28	const
HD 208674	229013861	1	rot?
HD 210780	206547467	1,28	rot?
HD 211993	441196602	1,28	const
HD 213155	139468902	1,28	rot
HD 218801	260820871	1,27-28	rot?
HD 218976AB	2055312708	1,28	rot
HD 22252	31867144	1,3,7,10,27-30,34,37	SPB? + rot?
HD 223118	33945685	2,29	rot?
HD 24579	238194921	1,2,9,13,27-29,32,39	SPB? / rot?
HD 26109	370038084	1-13,27-39	const
HD 29794	231099181	27-38	const
HD 30956	294867833	9-13,27-39	const
HD 32493	55746262	27-39	EV? / rot
HD 33244	140828939	28-36,38,39	rot?
HD 34376	257720864	27-37,39	SPB + rot
HD 34543	149039372	1-2,4-12,27-32,34-39	SPB + rot?
HD 37027	287435694	6,9,10,13,27-36,38,39	rot? + SPB?
HD 37066	149253686	27-37,39	EV? / rot
HD 37796	149388662	27-33,35-39	const
HD 37854	141281495	1-2,4-12,27-32,34-39	rot
HD 38974	149572666	27-39	const
HD 40435	31313111	4,28-29,31,32,34-36,38,39	rot
HD 41297	149971754	1-5,7-13,27-39	SPB
HD 42804	150102853	28-33,35,38,39	rot + SPB?
HD 42918	260128701	1-2,4-12,27-32,34-39	rot? + SPB / β Cep
HD 44247	41591173	27-35,37,38	EB
HD 44533	141828072	27-38	rot + δ Sct
HD 44577	150250617	27-39	rot?
HD 44937	260368525	1-9,11-13,27-39	rot?
HD 45527	167045028	1-7,9-13,27,29-37,39	rot
HD 45835	150360599	27-33,35-39	SPB
HD 46212	260540898	2,27-39	const
HD 46668	142014655	27-39	const
HD 46976	167248140	27-39	rot?
HD 47478	293268667	1-7,9-13,27-39	SPB
HD 47770	278683664	1-6,8-13,27-39	rot?
HD 48246	375057127	27-33,35-39	SPB
HD 48360	375038081	27-39	SPB
HD 48467	167415960	1-7,9,11-13,27-33,35-39	const
HD 48654	375061989	4-9,11,13,27-28,30-38	rot?
HD 48971	278865766	2-6,10-13,27-39	const
HD 49111	278867172	2,5-6,8-9,12,29,32-36,39	const
HD 49193	167523976	1-8,10-13,27-39	SPB / β Cep
HD 49306	176935619	1-9,11-13,28-36,38,39	rot?
HD 49339	176935871	28-36,38,39	SPB
HD 49424	176957187	27-35,37-39	SPB? / rot?
HD 49494	278898462	27-39	rot
HD 49531	176955379	1-3,5-13,27-30,32-33,35-39	SPB + rot?

Table 5: continued.

Name	TIC	TESS sectors	Photometry
HD 49692	176958810	27-39	const
HD 49835	270557257	1,3-8,10-13,27-28,30-35,37,38	const
HD 50903	279091621	27-30,32-39	rot? / SPB?
HD 51269	167694397	27-35,37-39	rot
HD 51555	279218413	27,29-39	SPB
HD 55478	300010961	1-9,11-13,27-39	rot + δ Sct
HD 56644	349156177	27-39	const
HD 57360	294399474	4-9,27-39	const
HD 57808	349310293	27-28,30-38	const
HD 57970	349311905	4-5,7-13,27-39	rot
HD 58916	300325379	1-2,4-12,27-32,34-39	rot?
HD 59426	300329728	1-3,5-13,27-33,35-39	rot
HD 59873	349576238	27-39	const
HD 61267	349829477	1,3-11,13,27-39	const
HD 61765	349909808	27-35,37-39	SPB
HD 62092	350024659	27-39	const
HD 63928	300744369	1-6,8-13,27-39	rot
HD 63969	281634192	27-39	rot?
HD 64186	382437069	27-35,37-39	rot?
HD 64484	300865934	1-2,4-12,27-32,34-39	const
HD 64811	410447919	1,4-5,7-11,13,27-28,30-38	SLF
HD 66109	364421326	1,4-5,7-11,27-28,31,34,35,37,38	const
HD 66591	308395911	1,4-5,7-11,27-28,31,34,35,37,38	SPB
HD 67170	308456810	1,4,7-11,28,31,34-38	const
HD 67252	306672432	1-9,11-13,27-39	rot?
HD 67277	308537791	1,4,7-8,10-11,31,34-37	EV? / rot?
HD 67299	272429196	27-30,32-39	SPB? + rot?
HD 67420	308454245	1-2,4-12,28,31-32,34-38	δ Sct
HD 67559	306739463	27-39	rot
HD 6783	182909257	1,13	rot
HD 68221	306824672	1-3,5-6,8-13,28-36,38,39	rot
HD 68423	308748912	1,4,8-11,28,31,34-38	const
HD 73990	307993483	2,9-12,29,32,36-39	rot
ι Vol	177075997	1-13,27,29-37,39	rot
κ Men	261205462	1,4-5,7-8,11-13,27-28,31-32,34,35,37-39	SPB
λ PsA	441182258	1,28	rot? + SLF?
μ Men	294747615	1-13,27-39	rot
μ Pic	260640910	1-6,8-13,27-39	SPB
θ Ret A	38602305	1-13,27-39	rot + SPB?
SB2 systems			
CCDMJ06125-6128AB	150165182	27-33,35-39	rot?
CCDMJ07395-7027AB	300708584	27-39	rot
ϵ Vol	805877893	1-6,8-13,28-33	SPB
HD 198174	270070443	1	rot
HD 20784	207235278	2-4,29-31	EV / rot?
HD 208433	152283270	1,28	const
HD 225119	12359289	2	rot
HD 269606*	279951435	27-28,30-38	SLF
HD 29994	231122278	1-4,6-13,27-34,36-39	rot
HD 32034*	30113151	27-38	SLF
HD 33599	55295028	1-13,27-39	rot + outburst + SPB
HD 35342B*	179209305	1-13,27,29-37,39	EB? / EV?
HD 45796	150357404	2-10,12-13,27,29-30,32-37,39	SPB
HD 47620	348841768	27-39	SPB
HD 48559	278823382	27-33,35-39	SPB
HD 53327	167814517	27-39	rot
HD 53921AB	766092864	1-13,27,29-37	rot
HD 54967	293973218	1-7,9-13,27-39	SPB
HD 56024	294205649	27-39	SPB
HD 62153AB	764642156	1,4-7,9-13,27-33	EV
HD 63204	350146577	1-13	rot

Table 5: continued.

Name	TIC	TESS sectors	Photometry
κ^1 Vol	307214534	2-3,5-6,9-13,29,32-33	EB / rot
AE Pic	150442264	1-3,5-13,27-30,32-33,35-39	EB + SPB
AN Dor	220430912	2-6,29-33,36,39	EB
V356 Car	372913684	1,4,7-11,27,31,34-37	rot
V455 Car	349907707	2,5-6,27-28,30-39	EB / EV + SLF

Table 6: Spectroscopic results for stars analysed with ZETA-PAYNE. “LPV” stands for line profile variations where we do not make a distinction between true nature of the observed variability, unless explicitly discussed in the text. “LPV*” are very narrow lined stars with strong line profile variations.

Name	N	S/N$_{max}$	Spectroscopy	T_{eff} (K)	ΔT_{eff} (K)	$\Delta_{\mathrm{i}} T_{\mathrm{eff}}$ (K)	$\log g$ (dex)	$\Delta \log g$ (dex)	$\Delta_{\mathrm{i}} \log g$ (dex)	$v \sin i$ (km/s)	$\Delta v \sin i$ (km/s)	$\Delta_{\mathrm{i}} v \sin i$ (km/s)	ξ (km/s)	$\Delta\xi$ (km/s)	$\Delta_{\mathrm{i}}\xi$ (km/s)	[M/H] (dex)	Δ [M/H] (dex)	Δ_{i} [M/H] (dex)
29 Dor	3	372	Be star	10819	36	432	3.88	0.02	0.12	182	10	16	0.6	0.4	2	-0.14	0.05	0.14
CD-60 1929	2	375	SB1	11833	49	433	3.9	0.02	0.12	64	4	13	0.0	0.4	2	+0.15	0.06	0.14
CD-60 1931	2	188	SB1	12254	59	434	3.83	0.03	0.12	178	11	16	3.6	1.3	2	-0.29	0.07	0.15
CD-60 1954	3	387	-	10997	30	431	4.28	0.02	0.12	193	8	14	2.8	0.5	2	+0.03	0.03	0.13
CD-60 1978	2	297	HgMn/LPV	11489	73	436	3.75	0.04	0.13	85	7	14	1.4	1.1	2	-0.42	0.12	0.18
CPD-60 944A	3	226	HgMn	12107	153	456	3.68	0.09	0.15	19	5	13	0.0	0.8	2	+0.11	0.12	0.18
CPD-60 944B	2	157	SB1/LPV*	11574	298	523	3.47	0.19	0.2	23	7	14	0.0	0.9	2	+0.45	0.13	0.18
η Phe	3	651	Be star	10243	24	431	4.00	0.02	0.12	115	6	13	1.2	0.3	2	+0.02	0.04	0.14
HD 1256	3	267	SB1	13181	77	437	3.95	0.02	0.12	173	11	16	3	2	3	-0.38	0.08	0.15
HD 201108	1	174	-	12216	64	435	3.97	0.03	0.12	125	11	16	1.1	0.7	2	+0.07	0.08	0.15
HD 208495	1	188	-	10430	39	432	4.28	0.03	0.12	70	5	13	0.5	0.3	2	+0.24	0.05	0.14
HD 208674	2	289	-	10443	24	431	4.19	0.02	0.12	141	7	14	2.1	0.5	2	-0.12	0.04	0.14
HD 210780	1	166	-	9391	53	433	4.24	0.03	0.12	173	16	20	4.3	0.9	2	-0.58	0.06	0.14
HD 211993	1	222	-	11151	39	432	4.01	0.03	0.12	173	10	16	0.8	0.4	2	+0.05	0.07	0.15
HD 213155	1	162	LPV	10169	37	432	4.09	0.03	0.12	94	7	14	0.3	0.3	2	+0.04	0.07	0.15
HD 218801	2	211	-	10862	40	432	4.1	0.03	0.12	111	7	14	1.0	0.4	2	+0.06	0.06	0.14
HD 218976AB	2	252	-	10587	24	431	4.31	0.02	0.12	202	11	16	3.1	0.6	2	-0.14	0.04	0.14
HD 22252	5	527	-	11810	37	432	3.46	0.02	0.12	237	7	14	1.6	0.9	2	-0.14	0.08	0.15
HD 223118	3	330	-	10840	25	431	4.43	0.02	0.12	261	11	16	5.8	0.9	2	-0.57	0.07	0.15
HD 24579	2	293	-	12892	71	436	3.76	0.03	0.12	109	9	15	0.8	0.7	2	-0.24	0.07	0.15
HD 26109	2	353	-	10026	37	432	4.44	0.03	0.12	108	41	43	4.1	1.0	2	-0.80	0.06	0.14
HD 29794	2	259	-	10521	28	431	4.12	0.02	0.12	128	8	14	1.8	0.5	2	-0.12	0.05	0.14
HD 30956	2	199	-	11753	60	434	3.98	0.03	0.12	206	10	16	3.9	0.9	2	-0.23	0.08	0.15
HD 32493	2	177	LPV*	8393	125	448	3.78	0.11	0.16	14	5	13	0.8	0.4	2	-0.16	0.13	0.18
HD 33244	3	393	-	11213	30	431	4.04	0.02	0.12	214	7	14	2.9	0.5	2	-0.13	0.04	0.14
HD 34376	2	291	-	13291	64	435	3.75	0.02	0.12	177	7	14	0.0	0.4	2	+0.26	0.04	0.14
HD 34543	3	298	-	11750	46	432	3.96	0.02	0.12	252	11	16	2.8	0.6	2	-0.31	0.07	0.15
HD 37027	3	372	Be star	10465	28	431	3.99	0.02	0.12	108	5	13	0.9	0.3	2	+0.21	0.05	0.14
HD 37066	3	360	-	13426	56	434	3.7	0.02	0.12	310	8	14	3.4	1.0	2	-0.38	0.06	0.14
HD 37796	2	237	LPV	10049	31	431	3.87	0.03	0.12	83	5	13	0.7	0.2	2	+0.06	0.05	0.14
HD 37854	3	349	-	10870	32	431	4.1	0.02	0.12	166	8	14	2.5	0.5	2	-0.04	0.04	0.14
HD 38974	3	254	-	11692	48	433	4.02	0.02	0.12	263	11	16	3.9	1.0	2	-0.53	0.07	0.15
HD 40435	2	233	LPV	9303	65	435	3.75	0.07	0.14	66	5	13	0.5	0.3	2	+0.35	0.06	0.14
HD 41297	2	214	LPV	12740	95	440	3.97	0.04	0.13	29	7	14	1.5	0.7	2	-0.27	0.08	0.15
HD 42804	2	228	LPV?	12824	77	437	3.35	0.03	0.12	117	9	15	0.6	0.9	2	-0.27	0.07	0.15
HD 42918	4	367	-	17951	155	457	4.2	0.03	0.12	159	6	13	1.6	0.9	2	-0.06	0.07	0.15
HD 44247	3	230	SB1/HgMn	12617	378	573	3.94	0.12	0.17	2	8	14	0.0	1.9	3	-0.1	0.2	0.3
HD 44533	3	360	Be star	12291	89	439	3.72	0.03	0.12	343	13	18	1.7	1.1	2	-0.41	0.08	0.15
HD 44577	3	324	-	11095	32	431	4.09	0.02	0.12	231	14	18	1.6	0.6	2	-0.30	0.05	0.14
HD 44937	3	306	-	10746	34	431	3.76	0.02	0.12	212	9	15	4.8	0.6	2	-0.16	0.04	0.14
HD 45527	2	190	LPV	11700	83	438	3.79	0.05	0.13	53	5	13	0.0	0.4	2	+0.32	0.06	0.14
HD 45835	2	206	-	11626	54	433	4.1	0.03	0.12	132	11	16	1.3	0.8	2	-0.01	0.08	0.15
HD 46212	3	336	-	11668	41	432	3.62	0.02	0.12	97	5	13	1.7	0.7	2	-0.78	0.07	0.15
HD 46668	2	165	-	11720	68	435	3.85	0.04	0.13	70	6	13	0.0	0.5	2	+0.28	0.05	0.14
HD 46976	3	246	-	11233	34	431	3.91	0.02	0.12	151	8	14	0.4	0.4	2	+0.07	0.05	0.14
HD 47478	2	355	-	11063	43	432	4.11	0.02	0.12	146	10	16	4.2	0.9	2	-0.36	0.09	0.16
HD 47770	3	342	-	10392	22	431	4.08	0.02	0.12	153	7	14	2.5	0.4	2	-0.14	0.03	0.13
HD 48246	3	346	SB1?	13720	66	435	3.58	0.02	0.12	296	9	15	3.3	1.0	2	-0.39	0.07	0.15
HD 48360	2	258	LPV	13832	98	441	4.14	0.03	0.12	45	14	18	2.2	1.6	3	-0.24	0.07	0.15
HD 48467	3	343	-	11614	44	432	3.98	0.02	0.12	96	4	13	2.6	0.6	2	-0.39	0.06	0.14
HD 48654	3	312	-	11832	43	432	4.17	0.02	0.12	182	8	14	1.3	0.4	2	+0.12	0.06	0.14
HD 48971	3	303	-	10512	25	431	3.98	0.02	0.12	114	6	13	1.6	0.4	2	-0.06	0.05	0.14

Table 6: continued.

Name	N	S/N$_{max}$	Spectroscopy	$T_{\rm eff}$ (K)	$\Delta T_{\rm eff}$ (K)	$\Delta_{\rm i} T_{\rm eff}$ (K)	$\log g$ (dex)	$\Delta \log g$ (dex)	$\Delta_{\rm i} \log g$ (dex)	$v \sin i$ (km/s)	$\Delta v \sin i$ (km/s)	$\Delta_{\rm i} v \sin i$ (km/s)	ξ (km/s)	$\Delta\xi$ (km/s)	$\Delta_{\rm i}\xi$ (km/s)	[M/H] (dex)	Δ [M/H] (dex)	$\Delta_{\rm i}$ [M/H] (dex)
HD 49111	3	297	-	10668	21	431	4.2	0.02	0.12	172	8	14	2.6	0.4	2	-0.15	0.04	0.14
HD 49193	2	206	SB1	21061	315	533	4.14	0.04	0.13	42	7	14	0.0	1.1	2	-0.16	0.07	0.15
HD 49306	3	353	-	10984	31	431	4.28	0.02	0.12	260	10	16	4.0	0.6	2	-0.16	0.04	0.14
HD 49339	2	225	-	14493	122	447	3.83	0.03	0.12	182	10	16	0.9	0.6	2	-0.11	0.07	0.15
HD 49424	3	316	HgMn/LPV	11898	56	434	4.1	0.03	0.12	73	5	13	0.3	0.4	2	+0.18	0.05	0.14
HD 49494	2	262	HgMn	11539	63	435	4.24	0.03	0.12	41	4	13	1.7	0.8	2	-0.42	0.08	0.15
HD 49531	2	208	-	11284	47	433	4.02	0.03	0.12	220	12	17	1.2	0.8	2	-0.08	0.09	0.16
HD 49692	2	264	-	11089	37	432	4.11	0.02	0.12	246	12	17	3.3	0.8	2	-0.19	0.05	0.14
HD 49835	2	269	-	10650	28	431	4.29	0.02	0.12	231	16	20	3.0	0.7	2	-0.38	0.06	0.14
HD 50903	3	333	SB1	12441	59	434	3.76	0.02	0.12	118	8	14	1.4	0.6	2	-0.28	0.06	0.14
HD 51269	2	239	HgMn	11379	137	451	3.68	0.08	0.14	14	4	13	0.0	0.6	2	+0.33	0.06	0.14
HD 51555	3	323	SB1/LPV	15784	136	451	4.24	0.03	0.12	33	5	13	10.3	1.5	3	-0.49	0.07	0.15
HD 55478	2	335	HgMn/LPV	13363	101	442	3.61	0.04	0.13	88	8	14	1.1	1.2	2	-0.28	0.10	0.16
HD 56644	3	349	LPV	10986	37	432	3.91	0.03	0.12	54	4	13	0.4	0.3	2	+0.11	0.05	0.14
HD 57360	2	241	SB1	10240	31	431	3.68	0.03	0.12	113	7	14	1.2	0.4	2	-0.18	0.06	0.14
HD 57808	3	245	HgMn	9744	79	437	3.64	0.07	0.14	2	4	13	0.8	0.3	2	+0.13	0.07	0.15
HD 57970	2	224	-	11926	59	434	3.85	0.03	0.12	70	5	13	0.0	0.4	2	+0.33	0.04	0.14
HD 58916	3	378	-	10951	28	431	3.97	0.02	0.12	230	10	16	1.6	0.5	2	-0.04	0.05	0.14
HD 59426	3	202	LPV*	10778	121	447	3.89	0.07	0.14	13	4	13	0.4	0.3	2	+0.42	0.07	0.15
HD 59873	2	301	-	10341	38	432	3.83	0.03	0.12	33	2	12	0.7	0.4	2	-0.03	0.07	0.15
HD 61267	3	256	-	10765	27	431	4.22	0.02	0.12	157	9	15	2.6	0.5	2	+0.00	0.04	0.14
HD 61765	3	337	SB1/LPV	13284	81	438	4.18	0.03	0.12	13	2	12	1.6	0.5	2	-0.13	0.05	0.14
HD 62092	3	340	-	11446	57	434	3.64	0.03	0.12	34	2	12	0.0	0.4	2	+0.00	0.10	0.16
HD 63928	2	233	LPV	10959	51	433	3.95	0.03	0.12	60	5	13	0.1	0.5	2	-0.33	0.08	0.15
HD 63969	2	278	-	11401	40	432	3.98	0.02	0.12	316	9	15	8.3	1.2	2	-0.73	0.06	0.14
HD 64186	3	311	SB1/LPV	11724	50	433	4.07	0.02	0.12	95	6	13	0.1	1.0	2	-0.3	0.2	0.2
HD 64484	3	415	-	10979	31	431	3.99	0.02	0.12	150	6	13	3.4	0.5	2	-0.14	0.05	0.14
HD 64811	3	242	-	14032	113	445	3.16	0.03	0.12	128	7	14	4.0	1.1	2	-0.04	0.07	0.15
HD 66109	3	282	-	11780	49	433	4.02	0.02	0.12	252	12	17	5.8	1.0	2	-0.36	0.07	0.15
HD 66591	3	637	-	17034	143	453	4.14	0.04	0.13	9	3	12	1.4	0.9	2	-0.07	0.07	0.15
HD 67170	3	325	HgMn	12227	89	439	3.67	0.04	0.13	36	4	13	1.0	0.8	2	-0.28	0.08	0.15
HD 67252	2	251	-	11237	44	432	4.09	0.02	0.12	112	12	17	4.1	1.3	2	-0.36	0.07	0.15
HD 67277	3	334	HgMn/LPV	12087	74	436	3.69	0.03	0.12	68	5	13	0.0	0.8	2	-0.32	0.11	0.17
HD 67299	3	298	-	11895	70	436	3.76	0.03	0.12	217	13	18	3.2	1.1	2	-0.25	0.10	0.16
HD 67420	3	277	-	11024	38	432	4.12	0.03	0.12	132	9	15	2.3	0.5	2	+0.07	0.05	0.14
HD 67559	3	395	HgMn	12214	120	446	3.47	0.05	0.13	49	6	13	0.0	0.9	2	-0.34	0.12	0.18
HD 6783	3	209	LPV*	10037	221	483	3	0.14	0.18	30	4	13	1.2	0.4	2	+0.79	0.09	0.16
HD 68221	2	227	-	11302	42	432	4.05	0.03	0.12	162	13	18	1.3	1.1	2	-0.16	0.08	0.15
HD 68423	3	381	Be star	13350	93	440	4.00	0.03	0.12	6	2	12	1.9	0.5	2	-0.46	0.05	0.14
HD 73990	4	369	-	10998	29	431	4.04	0.02	0.12	126	7	14	0.7	0.3	2	+0.05	0.04	0.14
ι Vol	3	457	-	11962	38	432	3.68	0.02	0.12	97	5	13	0.1	0.4	2	+0.05	0.05	0.14
κ Men	4	404	-	11292	30	431	4.09	0.02	0.12	248	9	15	2.4	0.6	2	-0.14	0.04	0.14
λ PsA	1	319	-	12274	68	435	3.72	0.03	0.12	61	4	13	0.0	1.9	3	-0.20	0.09	0.15
μ Men	3	452	HgMn	12199	175	464	3.58	0.06	0.13	26	3	12	0.0	0.6	2	+0.10	0.11	0.17
μ Pic	3	458	Be star	11081	31	431	3.76	0.02	0.12	203	8	14	1.0	0.3	2	-0.06	0.05	0.14
θ Ret A	3	470	HgMn	11492	82	438	3.76	0.04	0.13	44	5	13	0.0	0.7	2	-0.26	0.15	0.2